Complementing sparse vascular imaging data by physiological adaptation rules

american physiological society

JOURNAL OF APPLIED PHYSIOLOGY

J Appl Physiol 130: 571–588, 2021.
First published October 29, 2020; doi:10.1152/japplphysiol.00250.2019

INNOVATIVE METHODOLOGY

Complementing sparse vascular imaging data by physiological adaptation rules

Maarten H. G. Heusinkveld,[1] Robert J. Holtackers,[2] Bouke P. Adriaans,[3] Jos Op't Roodt,[4] Theo Arts,[1] Tammo Delhaas,[1] Koen D. Reesink,[1] and Wouter Huberts[1,5]

[1]*Department of Biomedical Engineering, Maastricht University, Maastricht, The Netherlands;* [2]*Department of Radiology and Nuclear Medicine, Maastricht University Medical Center, Maastricht, The Netherlands;* [3]*Department of Cardiology, Maastricht University Medical Center, Maastricht, The Netherlands;* [4]*Department of Internal Medicine, Maastricht University Medical Center, Maastricht, The Netherlands; and* [5]*Department of Biomedical Engineering, Eindhoven University of Technology, Eindhoven, The Netherlands*

Abstract

Mathematical modeling of pressure and flow waveforms in blood vessels using pulse wave propagation (PWP) models has tremendous potential to support clinical decision making. For a personalized model outcome, measurements of all modeled vessel radii and wall thicknesses are required. In clinical practice, however, data sets are often incomplete. To overcome this problem, we hypothesized that the adaptive capacity of vessels in response to mechanical load could be utilized to fill in the gaps of incomplete patient-specific data sets. We implemented homeostatic feedback loops in a validated PWP model to allow adaptation of vessel geometry to maintain physiological values of wall stress and wall shear stress. To evaluate our approach, we gathered vascular MRI and ultrasound data sets of wall thicknesses and radii of central and arm arterial segments of 10 healthy subjects. Reference models (i.e., termed RefModel, n = 10) were simulated using complete data, whereas adapted models (AdaptModel, n = 10) used data of one carotid artery segment only, and the remaining geometries in this model were estimated using adaptation. We evaluated agreement between RefModel and AdaptModel geometries, as well as that between pressure and flow waveforms of both models. Limits of agreement (bias ± 2 SD of difference) between AdaptModel and RefModel radii and wall thicknesses were 0.2 ± 2.6 mm and −140 ± 557 μm, respectively. Pressure and flow waveform characteristics of the AdaptModel better resembled those of the RefModels as compared with the model in which the vessels were not adapted. Our adaptation-based PWP model enables personalization of vascular geometries even when not all required data are available.

NEW & NOTEWORTHY To benefit personalized pulse wave propagation (PWP) modeling, we propose a novel method that, instead of relying on extensive data sets on vascular geometries, incorporates physiological adaptation rules. The developed vascular adaptation model adequately predicted arterial radius and wall thickness compared with ultrasound and MRI estimates, obtained in humans. Our approach could be used as a tool to facilitate personalized modeling, notably in case of missing data, as routinely found in clinical settings.

computational model; hemodynamics; imaging; sparse data; vascular adaptation

INTRODUCTION

Pulse wave propagation (PWP) models, as governed by the 1-D equations of momentum balance and mass conservation (1), describe propagation of pressure-flow waves within networks of (elastic) tubes. In cardiovascular research, PWP models have been applied to relate changes in blood flow characteristics [e.g., mean flow rate or systolic blood pressure (2)] to vascular pathologies, such as arterial stenosis (i.e., local narrowing of blood vessels) and aneurysms (i.e., pathological widening of blood vessels). PWP models are also used to predict the outcome of interventions in individual patients (3–6). Personalized clinical applications of PWP models require patient-specific clinical data to parameterize the model.

However, personalization of PWP models is usually hampered because only limited clinical data are available owing to time constraints, accessibility, procedural costs, or loss of data. One way to deal with sparse clinical data is to perform an extensive sensitivity analysis to help prioritize the PWP model parameters that require patient-specific measurements (7). Another option is to reduce model complexity, reducing the number of 1-D arterial branches within an arterial domain, by lumping them into less complex 0-D Windkessel models instead (8). Among caveats of lumping vascular networks into Windkessel is that the spatial information of the distributed arterial properties is lost (8). This hinders applications in which the model is used to assess amongst others peripheral to aortic transfer function, arterial parameters, heart-vessel

Correspondence: M. H. G. Heusinkveld (maarten@heusinkveld.nu).
Submitted 9 April 2019 / Revised 23 October 2020 / Accepted 27 October 2020

interactions, or optimal arteriovenous fistula configuration in patients with renal disease (2).

In the present paper, we propose a completely different and innovative approach to complement sparse data on arterial radius and wall thickness by utilizing knowledge of the adaptive capacity of the human vasculature in response to mechanical stresses.

Arteries are sensitive to changes in mechanical stresses. These changes typically drive normal development but also govern disease-related vascular adaptations, e.g., in hypertension (9). Within the arterial wall, several types of cells (i.e., vascular smooth muscle cells, fibroblasts, and endothelial cells) are sensitive to an offset in mechanical stress from homeostatic values (10). Two types of mechanical stress are relevant in this homeostatic process: wall shear stress (i.e., stress developed by friction of the blood flow at the blood-wall interface; order of magnitude of 1 Pa) and wall stress (i.e., stress in the vessel wall developed by transmural pressure; order of magnitude of 10^5 Pa) (11, 12). As a result of changes in wall (shear) stress, cells can mediate changes in the vessel wall by *1*) remodeling and/or turnover of cell products aiming to restore mechanical homeostasis and *2*) altering the vasoactive state of a vascular smooth muscle cell (10). At macrolevel, such adaptation processes affect arterial radius and wall thickness (9, 10, 13). We hypothesize that radius and wall thickness can be estimated by incorporating adaptation rules in the PWP model, which respond to wall shear stress and wall stress as generated by the model itself.

In the present analysis, we assess whether incorporating a model of the above-described adaptation processes into a validated PWP model (14) is beneficial for model personalization. To this end, a generic arterial tree describing the central arteries and the arteries of the left arm was considered. The generic tree was parameterized using generic data on arterial segment length and arterial radius, wall thickness, and wall stiffness (5, 15). Using measured data gathered from 10 young, healthy subjects, we first performed simulations using a reference PWP model fed by the entire clinical data set. Subsequently, simulations were performed using a PWP model with generic data, fed by a subset of the clinical data set. This subset contains subject-specific flow, distensibility, and pressure measurements, as well as a subject-specific radius and wall thickness for the left carotid arterial segment in the model. For all remaining arterial segments, radius and wall thickness were estimated by the adaptation model. Model-estimated tube geometries and pressure and flow waveforms were compared with the reference data. Additionally, a variance-based sensitivity analysis was conducted to quantify to which extent error in the model-estimated geometries, as well as in pressure and flow waveform characteristics, changed when varying the adaptation model parameters.

METHODS

Imaging and Hemodynamic Data

Ten young, apparently healthy volunteers (5 male, 25 ± 3 yr) were recruited to undergo ultrasound (US) and magnetic resonance imaging (MRI) examination. Exclusion criteria were smoking history or current smoking, diabetes, and the standard MRI contraindications, such as metallic devices and implants, epilepsy, pregnancy, and severe claustrophobia. The study was approved by the medical ethics committee of the Maastricht University Medical Center, and written informed consent was obtained from all volunteers before enrolment. A detailed description of data acquisition and processing steps is given in the APPENDIX, and a brief summary is given here.

Repeated oscillometric measurements of brachial blood pressure were obtained. Subsequently, applanation tonometric waveforms were obtained at the left common carotid, left brachial, and left radial artery. Local carotid and radial blood dynamic pressures were obtained by calibrating tonometric waveforms (16).

Two-dimensional longitudinal US recordings of the left brachial, left radial, left ulnar, and left common carotid artery were acquired using a US machine equipped with a 4- to 13-MHz linear array probe. Diastolic diameter and distension (i.e., difference between systolic and diastolic diameters) were automatically determined using built-in wall-tracking software. Doppler-based volume flow measurements were obtained at the brachial, radial, and ulnar artery. Wall thickness was measured for the carotid artery using dedicated software that automatically delineates media-adventitia echoes of near and far walls (Fig. 1).

Distensibility (D_0) of the brachial, radial, and carotid artery was estimated from ultrasound-based measurements of diastolic and systolic diameters in conjunction with the local blood pressure estimates.

All tonometric and ultrasound measurements were performed by a vascular research technician (J.O.R.).

Within 1 h after the US examination, noncontrast enhanced MRI was performed using a 3 T clinical magnetic resonance (MR) system (Ingenia CX, Philips Healthcare, Best, The Netherlands). First, a 3-D respiratory-navigated ECG-triggered T2-prepared turbo field echo sequence was performed, covering both the aortic arch with its branches and the ascending and descending aorta. After reconstructing this 3-D data into coronal, sagittal, and transversal views, 2-D imaging planes were selected perpendicular to the ascending aorta, brachiocephalic artery, left common carotid artery, left subclavian artery, and the descending aorta (Fig. 1). On each of these locations, both an anatomical scan (2-D black-blood turbo spin-echo) and a quantitative flow scan (2-D phase-contrast) were performed during breath hold. The anatomical scans were used to determine the lumen diameter of the vessels, which was measured from inner edge to inner edge, i.e., intima to intima, in both the anterior-posterior and right-left directions, and then averaged. Furthermore, we determined wall thickness for the ascending and descending aorta only. Sufficient contrast of the vessel wall that allows for accurate wall thickness assessment was obtained in only specific directions. When moving from the vessel center outward, these directions were found to be from the center of the vessel orthogonal to the medial, lateral, posterior, and anterior sides. In case two or more wall thicknesses could be determined, the average of these wall thickness measurements was taken. The quantitative flow scans were acquired with 25 cardiac phases in three velocity-encoding directions (right-left, anterior-posterior, and feet-head) using a velocity encoding (VENC) of 200 cm s^{-1}.

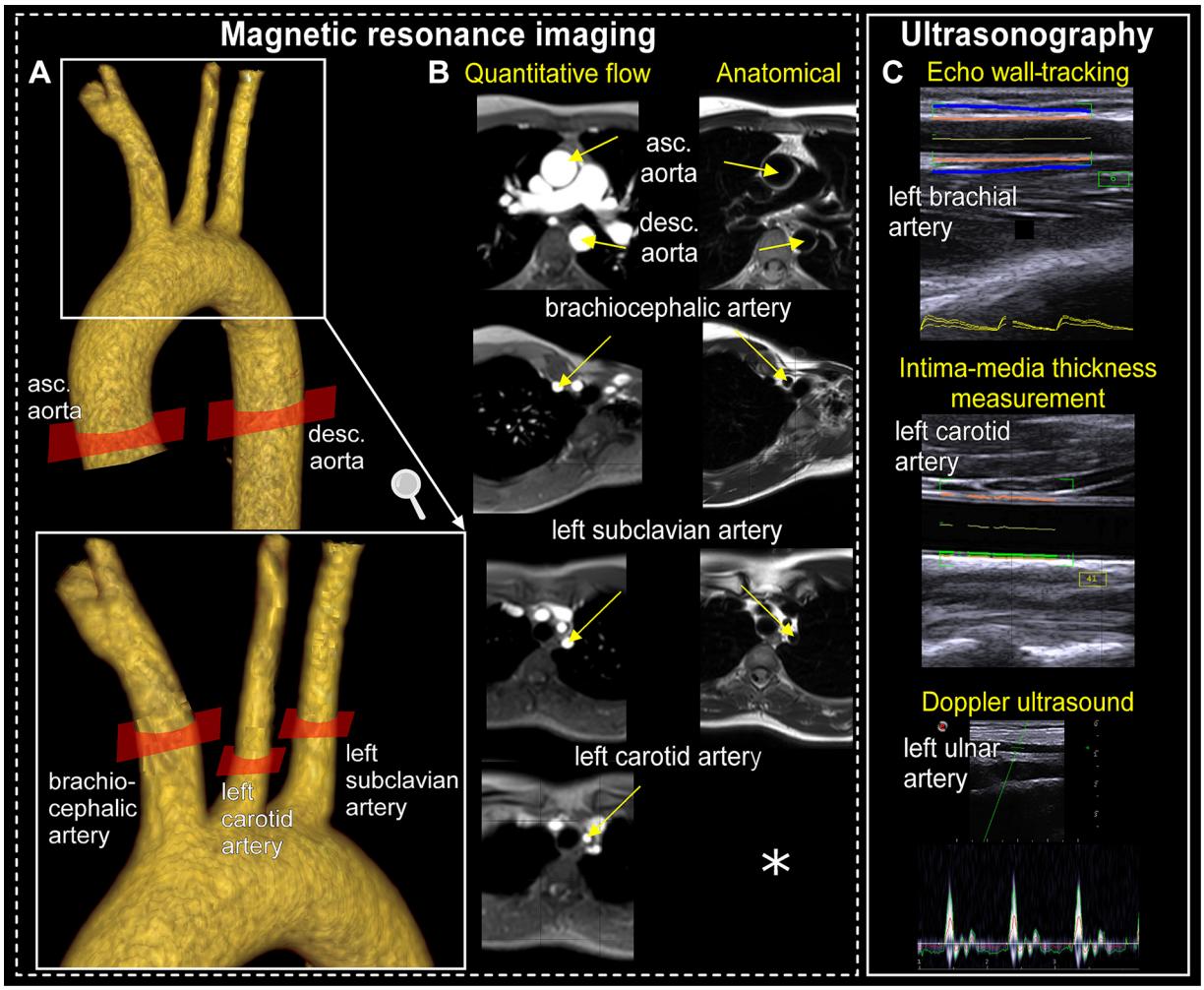

Figure 1. An example of the clinical data used. *A*: locations of scan planes for each measured artery (i.e., ascending aorta, descending aorta, brachiocephalic, left carotid, and left subclavian artery). *B*: quantitative flow images for the feet-head encoding direction (*left*) and anatomical images (*right*), as obtained for each scan plane. *C*: vascular ultrasonography measurements. *Indicates a different approach for the carotid artery, where carotid artery flow was acquired using MRI and carotid diameter was obtained by ultrasonography. The latter was chosen because of the superior spatial resolution of the ultrasound data over the MRI data.

Specific details of the used MR sequences are given in Table A1. All MR measurements were obtained by an experienced cardiac MR operator (R.J.H.), and the analysis of the vessel diameters and wall thicknesses was performed by an experienced reader (B.P.A.) at the Department of Cardiology.

Subject characteristics and measured variables are presented in Table 1. Data on vascular geometry, flow, and blood pressure were either directly obtained using the devices' built-in software or from offline analysis by trained investigators. Compliance (C_0) was assumed linear around reference pressure, p_0 (i.e., $C \approx C_0 = \frac{\partial A}{\partial p}|_{p=p_0}$) (5, 17). Distensibility (D_0) of the brachial, radial, and carotid artery was estimated from the actual compliance (C). It then follows that distensibility can be approximated using ($D_0 = C_0/A_0$). Substitution of $C_0 = \Delta A/\Delta p$ into the aforementioned equation yields $D_0 = \Delta A/\Delta p A_0$. Note that we can obtain ΔA from vascular ultrasound measurements and Δp from pressure and tonometry measurements. Given these assumptions, we may write

$$D_0 = \frac{C_0}{A_0} \approx \frac{1}{\pi r_0^2}\frac{\Delta A}{\Delta p} \approx \frac{r_{sys}^2 - r_{dia}^2}{r_0^2 \Delta p} \quad (1)$$

Here, A_0 represents reference lumen area, expressed as πr_0^2, where r_0 is the arterial radius at mean arterial pressure. The radii r_{sys} and r_{dia} are the systolic and diastolic radii, respectively, and Δp is the local pulse pressure.

Model Description

Pulse wave propagation model.

A validated PWP model (14) was used to compute pressure (p) and flow (q) waveforms within a network of systemic vessels describing large central arteries and the middle- to smaller-size arteries of the left arm (Fig. A1). A detailed mathematical description of this model is provided in the APPENDIX.

Adaptation model.

The adaptation model is based on two phenomena, as observed in vascular physiology. On the one hand, we

Table 1. *Overview of characteristics and measured variables in 10 subjects*

Subject Characteristics	A	B	C	D	E	F	G	H	I	J
Age, yr	26	23	27	25	25	30	27	22	20	27
Sex, m/f	m	m	f	f	m	f	m	f	f	m
Height, m	1.87	1.81	1.79	1.71	1.77	1.76	1.81	1.68	1.73	1.81
Weight, kg	68	60	90	68	69	66	69	56	63	68
Heart rate, beats/min	85	57	60	68	61	72	47	35	76	68
Arterial diameters, mm										
Ascending aorta	31.6	25.9	24.3	22.7	28.1	32.5	24.5	20.9	23.5	27.6
Descending aorta	20.5	19.5	19.6	17.2	20.9	19.3	20.8	13.5	15.3	18.2
Left carotid artery	6.8	6.6	7.8	7.4	7.2	7.3	7	7	6.4	6.9
Brachiocephalic artery	11.3	10.3	12.9	10.6	10.6	12.7	10.6	6.3	12.2	11.3
Left subclavian artery	9.3	9.3	8.3	7.8	9.4	7.1	7.4	4.6	8.2	9.3
Left brachial artery	4.8	4.2	3.9	3.1	4.5	3.2	3.4	3.5	3.1	4.7
Left radial artery	2.7	2.7	2.2	1.7	2.8	2.4	2.4	2.3	1.6	2.8
Left ulnar artery	3	2.6	2.4	3.6	3.5	2.8	2.9	2.2	1.6	3.2
Arterial distension, μm										
Left carotid artery	581	888	692	624	851	618	674	966	826	634
Left brachial artery	149	133	145	316	88	28	101	95	54	213
Left radial artery	35	56	35	24	29	26	40	19	23	33
Left ulnar artery	61	73	53	71	66	27	35	17	24	63
Arterial wall thickness, μm										
Ascending aorta	1,440	1,430	2,050	1,180	1,690	1,710	1,500	1,220	1,500	1,700
Descending aorta	1,280	1,260	1,270	1,330	1,490	1,440	1,560	900	1,030	1,520
Left carotid artery	441	398	472	603	562	574	589	556	353	412
Mean flow, mL/min										
Ascending aorta	8,722	5,570	6,255	6,897	6,810	7,449	3,636	3,194	5,973	6,306
Descending aorta	5,477	4,447	3,175	4,798	4,952	5,928	2,738	1,823	3,863	4,488
Brachiocephalic artery	1,171	734	730	1,130	1,203	1,192	518	718	751	934
Left carotid artery	382	259	290	276	395	339	325	260	382	446
Left subclavian artery	657	346	526	472	408	622	232	173	413	444
Left radial artery	20	23	6	6	9	13	20	9	7	24
Left ulnar artery	22	23	4	20	32	14	75	8	6	14
Distensibility, 10^{-6} Pa^{-1}										
Left carotid artery	30.6	41.8	35.2	43	62.2	60.8	32.7	52.7	47.8	29.7
Left brachial artery	9.6	8.3	11.5	38.3	5.4	7.2	7.2	9	7.3	12.4
Left radial artery	3.1	4.7	7.5	4.8	4.5	11.8	4	1.8	3.5	2.6
Systolic/diastolic pressure, mmHg										
Left brachial artery	123/74	111/54	129/79	112/60	110/55	104/63	128/65	106/58	120/68	156/92
Left carotid artery	118/74	106/54	118/79	94/60	86/55	86/63	112/65	101/58	115/68	142/92
Left radial artery	138/74	121/54	133/79	115/60	109/55	101/63	130/65	129/58	134/68	161/92
Mean pressure, mmHg										
Left brachial artery	94	74	96	75	67	63	84	75	87	111

consider wall thickness adaptation due to changes in wall stress. Earlier work showed that increased wall stress due to induced hypertension in rats is associated with a progressive increase in wall thickness, eventually resulting in normalization of wall stress to that during a normotensive state (9).

The increase in wall thickness has been attributed to vascular smooth muscle cell hypertrophy, hyperplasia, and increased amounts of elastin and collagen (9, 11). On the other hand, we consider vessel radius adaptation due to changes in wall shear stress (18). These changes are sensed by endothelial cells that modulate vascular smooth muscle cell tone, resulting in vasoconstriction or vasodilation through nitric oxide production or washout (10, 19). If changing vascular tone is insufficient to normalize wall shear stress, turnover of cell products will cause the artery to structurally adapt (10).

Vessel wall thickness adaptation.

Wall thickness adaptation is known to occur in response to changes in arterial wall stress with respect to some homeostatic target wall stress, e.g., induced by long-term changes in transmural arterial pressure (20, 21). Several researchers therefore modeled wall thickness adaptation based on this hypothesis. However, the exact mechanism is still unknown, and the exact homeostatic target wall stress for both arteries and veins remains to be determined. Particularly, it is not established yet which component of transmural pressure (mean, systolic, diastolic, or peaks/transients in pressure, or a combination of these) is responsible for triggering adaptation. Central larger veins and arteries have a comparable radius and wall thickness and carry a comparable flow, but these have a distinctly different transmural pressure (21). With a single wall stress target value, the resultant wall thickness adaptation in either the veins or arteries would lead to unphysiological geometries. Therefore, in the present study, we aimed for a single rule to govern adaptation of both arteries and veins (or shunts), with only one single homeostatic target value for both arteries and veins. To this end, we also considered pressure components other than the hydrostatic to estimate wall shear stress triggers for wall thickness adaptation. In the previous work, we showed that this approach resulted in physiologically realistic wall thickness adaptations in both arteries and veins (20, 22). Moreover, it was found that our approach allows simulation of vascular

growth or adaptation, with larger vessels responding to model-generated local hemodynamic conditions (22). It should be noted here that our adaptation rule considers only the vessel level rather than the underlying and more complex constitutive and mechanobiological aspects, which are clearly different for arteries and veins (21).

Our modeling approach was as follows: Cross-sectional wall area (A_{wall}) was changed in response to a relative deviation of peak wall stress (σ_f) from a target peak wall stress ($\sigma_{f,target}$). The change in A_{wall} is described by the following equation:

$$A_{wall,n+1} = \left(\frac{\sigma_{f,n}}{\sigma_{f,target}}\right)^{k_A} \cdot A_{wall,n}. \quad (2)$$

where n denotes the current adaptation cycle, and constant $k_A > 0$ governs the rate of adaptation. Note that vessel wall thickness (h) follows from cross-sectional wall area and vessel radius using $h = \sqrt{\frac{A_{wall}}{\pi} + r^2} - r$. According to our adaptation rule, wall thickness is determined by the maximum pressure (p_{max}), being the sum of the component due to peak pressure and a component related to whole body acceleration, e.g., occurring during moderate jumping. The value of $\sigma_{f,target}$ was chosen equal to 400 kPa so that the resulting wall thickness in the circulatory system is physiologic (20). The incorporation of the acceleration term is as follows. The expression for p_{max} is obtained, assuming that inertia forces dominate over viscous forces:

$$p_{max} = \max(p) + \max(Z_0 \cdot A) \cdot v_{impact}, \quad (3)$$

where p is the blood pressure, Z_0 is the vessel's characteristic impedance, and A is the vessel's lumen area. As a zero-order approximation, we assume that a body jump from 0.5-m height may induce an additional impact on the vessel wall that still can be resisted. We based this height on earlier studies on human vertical jumping agility (23). At impact, assuming no initial velocity and drag, body velocity v_{impact} is $\approx \sqrt{2gh} \approx 3.0\,m\,s^{-1}$. Now we have found a first-order approximation of p_{max}, and we are able to derive an expression for σ_f. Assuming blood vessels to be fiber-reinforced shells for which homogeneity of mechanical load within the wall holds, wall stress (σ_f) can be related to internal pressure (p) and the ratio of cavity to wall volume (V/V_{wall}) using the expression given by (20).

$$\sigma_f = \beta_1 p_{max}\left(\frac{V}{V_{wall}} + \beta_2\right), \quad (4)$$

where β_1 and β_2 are dimensionless constants. We adopted $\beta_1 = 3$ and $\beta_2 = 0.5$ (4). Substituting Eq. *3* in Eq. *4* and dividing by the length of the vessel segment yield the following expression for σ_f:

$$\sigma_f = 3\left(\max(p) + \max(Z_0 \cdot A) \cdot v_{impact}\right)\left(\frac{\max(A)}{A_{wall}} + \frac{1}{2}\right), \quad (5)$$

Vessel radius adaptation.

We assumed changes in mean wall shear stress to be the driving factor for vessel radius adaptation. An expression for mean wall shear stress is given by

$$\bar{\tau}_w = \frac{4\eta\bar{q}}{\pi r^3}, \quad (6)$$

where $\bar{q}$ is the mean flow rate. Vessel radius (r) was changed in response to a relative deviation of mean wall shear stress ($\bar{\tau}_w$) from a target wall shear stress ($\bar{\tau}_{w,target}$):

$$r_{n+1} = \left(\frac{\bar{\tau}_{w,n}}{\bar{\tau}_{w,target}} \cdot (1 + r_{crit}/r_n)\right)^{k_r} \cdot r_n. \quad (7)$$

Here, $k_r > 0$ is the adaptation rate constant for radius adaptation. For large blood vessels, Murray's law is known to describe well the radii of consecutive branches in a tree-like structure, when assuming local adaptation to a single wall shear stress set point. However, with decreasing radius also local fluid dynamics and hence rheological properties change, which lead to deviations from the rule (24). Therefore, we included in our rule the $(1 + r_{crit}/r_n)$ term to implement that modeled vessels with a radius smaller than a preset critical value (r_{crit}) adaptation significantly deviate from the rule. We set r_{crit} to 0.45 mm based on earlier reports on vascular smooth muscle cell length and their organization within the arterial wall (25). We considered separate target wall shear stress values for central (denoted $\bar{\tau}_{w,target,prox}$) and distal (denoted $\bar{\tau}_{w,target,dist}$) arteries. For central arteries, represented in the model by tubes 1 to 8, we chose $\bar{\tau}_{w,target,prox}$ 0.3 Pa (26, 27). For distal arteries, represented in the model by tubes 9, 10 and 12 to 18, $\bar{\tau}_{w,target,dist}$ was chosen 0.4 Pa (12, 28).

Simulations and Analysis

To assess the potential of our approach in completing sparse data sets, we performed three sets of simulations: *1*) the PWP model without adaptation, but fed with the complete clinical data set; *2*) the PWP model including adaptation, using a subset of the clinical data as input; and *3*) simulations to evaluate the effect of adaptation model parameters on output metrics. Details of these three analyses are given below.

RefModel.

To obtain the reference PWP models (referred to as the RefModel; Fig. 2), we prescribed for each subject:

1) The radius and wall thickness of all 18 modeled tubes. For measured segments, we imputed measured values. For arterial segments that were not measured, we obtained estimates by applying a scaling for radius (Table A2) and for wall thickness. For tube radius, we calculated a scaling factor determined from the ratio between the measured diameter of the left subclavian artery and its generic value (15). To estimate wall thickness, we used vessel-specific ratios between wall thickness and radius (i.e., the ratio h/r), assumed 0.10 for the aortic segments, 0.15 for the brachiocephalic, vertebral artery, and brachial artery, and 0.20 for the radial and interosseous artery (5).

2) Ascending aortic flow rate ($q_{in}(t)$), obtained using PC-MRI, to the proximal node of tube 1.

3) The flow distribution to the periphery, as derived from PC-MRI and Doppler measurements. Since flow measurements for the interosseous artery were absent, we assigned the same flow fraction to the interosseous artery as for the ulnar artery.

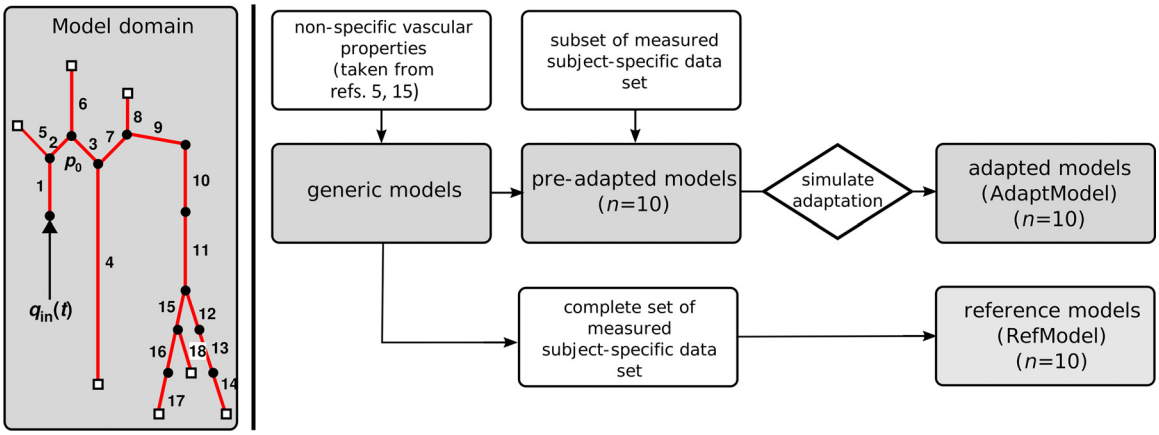

Figure 2. *Left*: arterial segments: 1 to 4: ascending, proximal arch, distal arch, thoracic aorta, 5: brachiocephalic, 6: carotid, 7: subclavian, 8: vertebral, 9 to 11: subclavian + brachial proximal, middle, distal brachial, 12 to 14: proximal, middle, distal radial, 15 to 17: proximal, middle, distal ulnar, 18: interosseous. p_0 denotes the subject-specific mean pressure and q_{in} the subject-specific inflow profile. *Right*: schematic overview of the simulation protocol used for obtaining the RefModel and AdaptModel of each subject.

4) Reference pressure (p_0) using the mean pressure measured at the brachial artery.

5) Young's modulus of the subclavian, axillary, brachial, ulnar, radial, and interosseous artery. Using Eq. *A5*, the measured D_0 was translated to a Young's modulus, to obtain material stiffness values for the brachial, radial, and carotid arterial walls. For the subclavian and axillary arteries, we imputed Young's modulus of the brachial artery, whereas for the ulnar and interosseous arteries in the model, we imputed Young's modulus of the radial artery.

All other model parameters were kept at generic values as given in Table A2.

AdaptModel.

To obtain the adapted PWP models, referred to as the AdaptModel (Fig. 2), from the generic model (Table A2) we used the following approach. First, we prescribed the subset of the data, as described in *steps 2 to 5* in the previous section, and in addition, the radius and wall thickness of the left carotid artery, to obtain preadapted models (Fig. 2). We then initiated the PWP adaptation procedure on the preadapted models, to estimate vessel radius and wall thickness for all arteries in the model except the left carotid artery.

Supporting simulations.

Three sets of supporting simulations were performed to characterize the adaptation model performance in detail. First, we evaluated whether adaptation model–predicted geometries converged to unique values. Second, pressure and flow waveforms were generated by the AdaptModel to waveforms generated by the RefModel, taking into account the influence of measurement error of the reference data. Third, an analysis on the sensitivity of adaptation model parameters ($\sigma_{f,target}$, $\bar{\tau}_{w,target,prox}$, $\bar{\tau}_{w,target,dist}$, r_{crit}, and v_{impact}) on hemodynamic indices was performed. Methodological details of these analyses are provided in the APPENDIX. Briefly, we expressed parameter sensitivities using main and total sensitivity indices (29). The main sensitivity index (S_i) represents the expected reduction in output variance (uncertainty) when the exact value of parameter "X" is known exactly. In essence, it quantifies the contribution of a single parameter on its own to the total output variance and can be used to decide which model parameter is most relevant to determine more accurately (parameter prioritization). The total sensitivity index (S_T) is the expected variance that remains if all parameters are exactly known except parameter "X." This index considers also interactions and can be used to determine which parameters are nonimportant (i.e., parameter fixing). Furthermore, output variance (a measure of output uncertainty) was also calculated using the simulation runs we needed to determine the sensitivity indices.

Metrics for agreement between AdaptModel and RefModel.

Agreement between model-estimated and reference radius and wall thickness, as well as between AdaptModel and RefModel pressure and flow waveforms, was quantified using the root- mean–square errors given by

$$\epsilon_r = \sqrt{\frac{\sum_{i=1}^{N}(r_{ref} - r_{mod})^2}{N}},$$
$$\epsilon_p = \sqrt{\frac{\sum_{i=1}^{N}\left(p_{ref,median}(t) - p_{mod}(t)\right)^2}{(T/\Delta t)}} \quad (8)$$
$$\epsilon_h = \sqrt{\frac{\sum_{i=1}^{N}(h_{ref} - h_{mod})^2}{N}},$$
$$\epsilon_q = \sqrt{\frac{\sum_{i=1}^{N}\left(q_{ref,median}(t) - q_{mod}(t)\right)^2}{(T/\Delta t)}}$$

Here, r_{mod} and h_{mod} represent model-estimated radius and wall thickness, and r_{ref} and h_{ref} represent reference radius and wall thickness, respectively. Furthermore, p_{mod} and q_{mod} represent model-estimated pressure and flow waveforms, respectively. The waveforms $p_{ref,median}$ and $q_{ref,median}$

represent reference pressure and flow waveforms, respectively, calculated as the median of the 40 RefModel realizations. Term $(T/\Delta t)$ denotes the number of data points per cycle and N the number of tubes. Only tube geometries based on actual measurements were included in the calculation of ϵ_r (i.e., tubes 1, 4, 5, 7, 10, 13, and 16) and ϵ_h (i.e., tubes 1 and 5).

Comparison with simple scaling rule.

As a final evaluation to establish the merit of our adaptation rule approach, we compared our outcomes with a simple scaling rule. We obtained scaling factors by using the following procedure. For each subject, we used the measured carotid artery radius and wall thickness (as given in Table 1) and derived age-adjusted radius and wall thickness, based on published regression models for radius and wall thickness versus age (30, 31). Subsequently, for each subject, a scaling factor was calculated based on the actually measured carotid artery radius and wall thickness, on the one hand, and the literature-derived ones, on the other hand:

$$r_{\text{scaling factor}} = \frac{r_{\text{carotid, measured}}}{r_{\text{carotid, literature}}}, \qquad (9)$$

$$r_{\text{scaling factor}} = \frac{r_{\text{carotid, measured}}}{r_{\text{carotid, literature}}}.$$

These scaling factors were subsequently used to scale the remaining arterial radii and wall thicknesses of all other blood vessels in the model domain. Table 2 shows *1*) typical values derived from the literature; *2*) actual values, measured in this study using ultrasonography; and *3*) scaling factors calculated as described above. We applied these scaling factors to our generic arterial domain, and we quantified the agreement between the resulting arterial radii and wall thicknesses, and measured data.

Source Data and Code

Source data are available as an electronic supplement. The computational model and sensitivity analysis code will be made available by the authors upon reasonable request.

RESULTS

Convergence to Unique Vessel Geometry

Initiating the PWP adaptation framework from 10 sets of take-off geometries around values given in Table A2, our adaptation framework resulted in negligible variations in adapted radius and wall thickness. The coefficient of variation (i.e., the standard deviation of the ten adapted geometries divided by their respective mean and expressed as a percentage) for tube radius was $\leq 4 \times 10^{-4}$% and that for wall thickness was $\leq 2 \times 10^{-1}$%.

Agreement between Model-Estimated and Reference Geometry

Figure 3 illustrates for two subjects the comparison between reference radius and wall thickness (black squares and whiskers) and model estimations of radius and wall thickness (red asterisks).

For the subjects presented in Fig. 3, errors in estimation of radius and wall thickness were small as evidenced by ϵ_r of 0.83 and 1.13 mm and ϵ_h of 136 and 150 μm, respectively. The radius and wall thickness of proximal arteries, representing the segments of the aorta, were also reasonably captured by the adaptation framework (Fig. 3). In Fig. 4, agreement between estimated radius and wall thickness, on the one hand, and reference data, on the other hand, is shown for all subjects (n = 10).

Agreement was quantified only for the arteries for which the radius (i.e., tubes 1, 4, 5, 7, 10, 13, and 16) and wall thickness (i.e., tubes 1 and 5) was measured. Limits of agreement (i.e., bias ± 2 SD of the difference) were 0.2 ± 2.6 mm for radius and −140 ± 557 μm for wall thickness.

Additionally, the agreement between generic tube geometries (Table A2) and subject data was inferior to that of the model-estimated ones, as described by limits of agreement of 1.6 ± 3.4 mm for radius and 0.5 ± 624 μm for wall thickness.

Pressure and Flow Waveforms

Figure 5 exemplifies by *subject A* the results on pressure and flow waveforms of the aorta, carotid artery, and radial artery.

Pressure and flow waveform characteristics (i.e., mean, diastolic, and systolic values) generated by the AdaptModel^A agreed with the ranges found using the RefModel^A. Furthermore, p and q waveforms for central arteries appear similar compared with those for median reference waveforms (ϵ_p = 1.5 mmHg and 1.4 mmHg and ϵ_q = 7.6 mL·s^{-1} and 0.3 mL·s^{-1}; Fig. 5). For the distal segment of the radial artery, p and q waveforms increasingly differed from the median reference waveforms (ϵ_p = 9.2 mmHg and ϵ_q = 0.1 mL·s^{-1}; Fig. 5). For the preadapted model, fed with subject-specific data but with generic vascular geometries, pressure and flow waveform (characteristics) significantly differed from the RefModel^A.

Table 2. *Derivation of simple scaling values to evaluate our model adaptation approach*

Subject	Age, yr	Literature Carotid IMT, μm	Literature Carotid Radius, mm	Actual Carotid IMT, μm	Actual Carotid Radius, mm	$h_{\text{scalingfactor}}$	$r_{\text{scalingfactor}}$
A	26	549	3.65	441	3.40	0.80	0.93
B	23	531	3.57	398	3.30	0.75	0.92
C	27	555	3.67	472	3.90	0.85	1.06
D	25	543	3.62	603	3.70	1.11	1.02
E	25	543	3.62	562	3.60	1.03	0.99
F	30	573	3.74	574	3.65	1.00	0.98
G	27	555	3.67	589	3.50	1.06	0.95
H	22	525	3.55	556	3.50	1.06	0.99
I	20	513	3.49	353	3.20	0.69	0.92
J	27	555	3.67	412	3.45	0.74	0.94

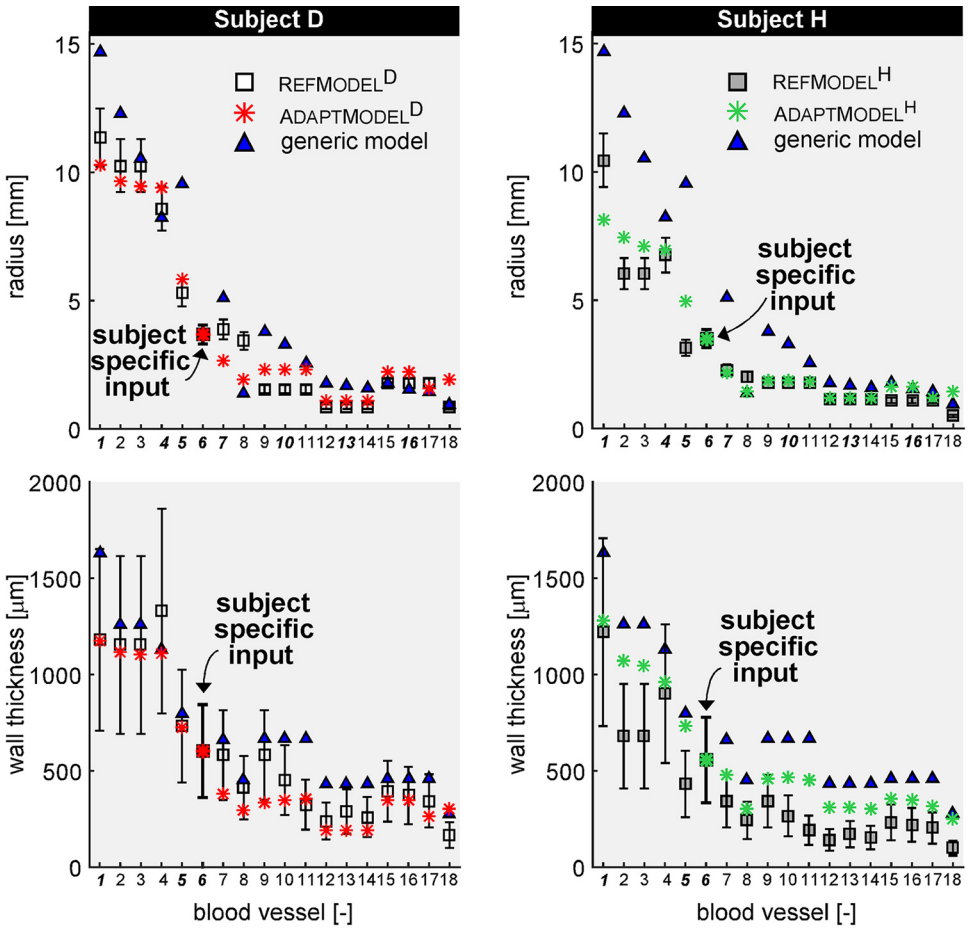

Figure 3. Comparison of the reference radius and wall thickness (RefModel^D and RefModel^H, squares with whiskers, respectively), generic values (triangles), and model-estimated tube geometries (AdaptModel^D and AdaptModel^H, asterisks) for *subjects D* and *H*, respectively. Whiskers indicate assumed measurement uncertainty of ±10% for radius and ±40% for wall thickness (55). Blood vessel numbers correspond to those depicted in Fig. A1. ϵ_r and ϵ_h represent root mean square errors between measured and model predicted radius and wall thickness. Bold italic values on the horizontal axes refer to vessels for which actual vessel radius and wall thickness measurements were obtained.

For all subjects, pressure and flow waveforms generated by the AdaptModel were in better agreement with reference pressure and flow waveforms, as compared with those generated by the preadapted model. This is illustrated by the significant reduction of, on the one hand, ϵ_p at the aorta by 49% (i.e., from 7.4 to 3.8 mmHg) and, on the other hand, by the reduction in ϵ_q by 36% (i.e., from 7.8 to 5.0 mL·s^{-1}), when adapting the vessels (Fig. 6).

Sensitivity of Hemodynamics and Vessel Geometry to Adaptation Model Parameter Variance

Main (S_i) and total (S_T) sensitivities are given in Table A3. The presented variances (VAR) may be interpreted as an uncertainty measure.

Systolic and diastolic blood pressure was particularly sensitive for the wall shear stress target value of proximal arteries ($\bar{\tau}_{w,target,prox}$, S_is between 0.77 and 0.99). High total sensitivities ($S_T > 0.82$) and relevant (i.e., 59 to 261 mmHg^2) variance values for each of these hemodynamic indices indicate the necessity of establishing reliable estimates for $\bar{\tau}_{w,target,prox}$.

Pulse wave velocity was sensitive to the wall shear stress target parameter, for both proximal arteries (S_i = 0.41) and distal arteries (S_i = 0.18). Variance in pulse wave velocity was 0.24 (m s^{-1})^2, which corresponds to a standard deviation of $\sqrt{0.24}$ = 0.49 m s^{-1}.

Blood pressure amplification showed moderate sensitivity for the wall shear stress target value of proximal arteries (S_i = 0.075) and the critical vessel radius (S_i = 0.23). Here, variance of Δp_{amp} was 0.027.

The root mean square error for the estimation of radius (ϵ_r) was only sensitive for the target wall shear stress value of proximal arteries (S_i = 0.99). Interestingly, this metric was not sensitive for the target wall shear stress value for distal arteries nor for critical vessel radius. The associated variance for ϵ_r was 0.126 m^2.

The root mean square error for the estimation of wall thickness (ϵ_h) was sensitive for both the target wall stress (S_i = 0.51) and v_{impact} (S_i = 0.097). The associated variance for ϵ_r was 0.0169 m^2. Note that several adaptation parameters are also involved in interactions with other parameters ($S_T - S_i > 0$), which advocates for the global sensitivity analysis approach.

Comparison with Simple Scaling Rule

Figure A4 illustrates the Bland–Altman agreement between measured radius and wall thickness values and those obtained by applying a simple scaling rule.

Table 3 compares the bias and limits of agreement between the adaptation rule and simple scaling rule

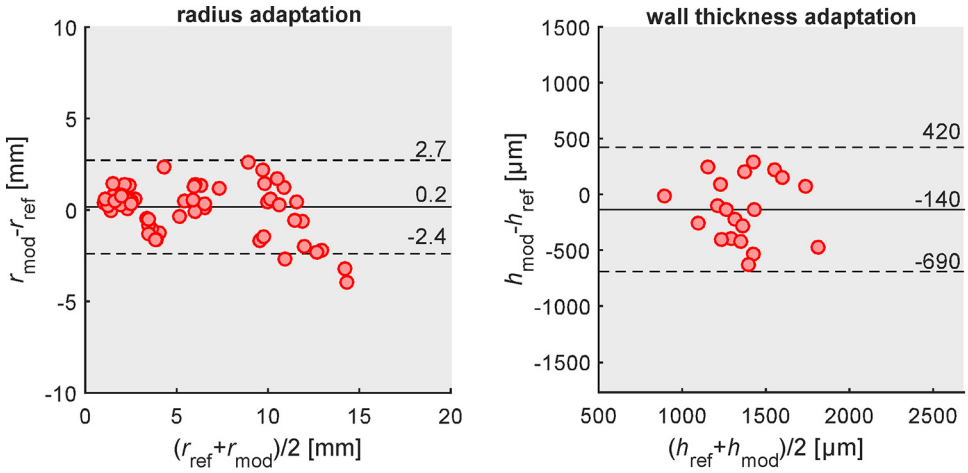

Figure 4. Bland–Altman plots of agreement between model-estimated and measured radius (*r*) and wall thickness (*h*). Values denote bias and limits of agreement (i.e., bias ± 2 SD of difference) between model estimations and measured data, respectively.

approaches. For both radius and wall thickness, the adaptation rule shows narrower limits of agreement, i.e., less variability of the estimates. Moreover, for radius the bias was ~7 times smaller for adaptation than for scaling.

DISCUSSION

The present study demonstrates the feasibility of predicting vessel geometry by incorporating vascular adaptation in a computational model of pulse wave propagation. This feasibility comes much at hand if confronted with sparse data sets on vessel geometry. Adaptation was based on the ability of vascular cells to sense perturbations in wall stress and wall shear stress and to mediate adaptation of vessel geometry to maintain mechanical homeostasis. A comparative evaluation between our adaptation approach and reference data demonstrated good agreement for geometry as well as pressure and flow waveforms along the modeled arterial domain.

Some aspects regarding our modeling assumptions warrant discussion. First, our model of radius adaptation is based on the hypothesis of constant mean wall shear stress regulation. The choice for mean wall shear stress was based on experimental work performed in dogs, studying the wall shear stress-radius relation under chronic increases in carotid artery flow. At 6 to 8 mo after the procedure, arterial remodeling caused lumen radius to increase, causing

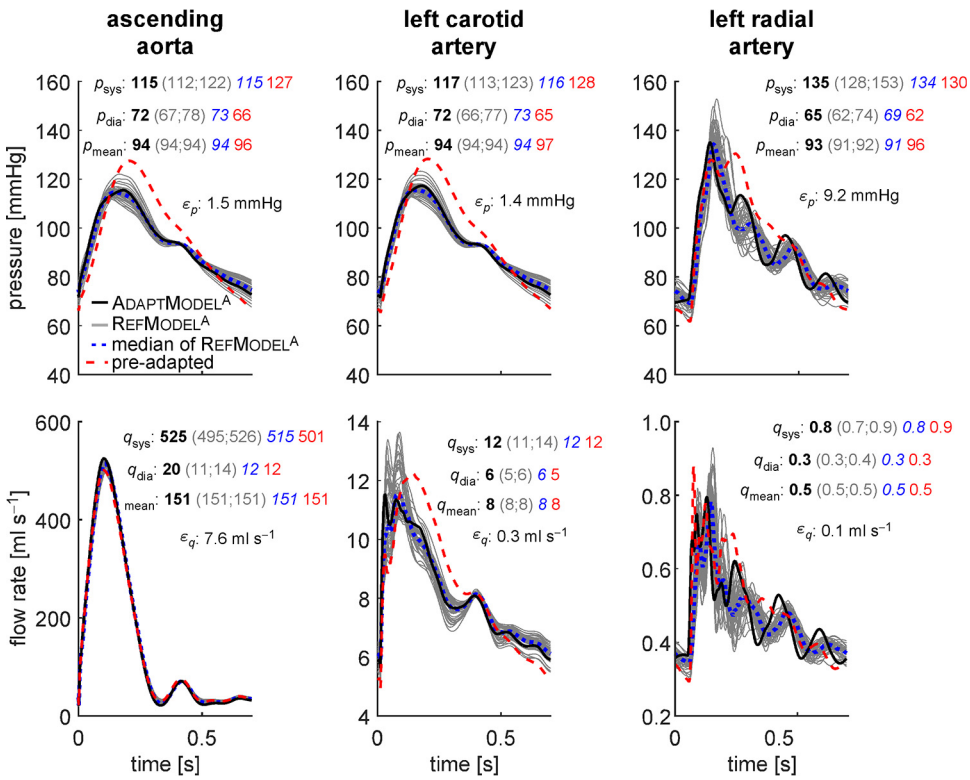

Figure 5. Pressure (*p*) and flow (*q*) waveforms for *subject A* at three locations, i.e., the aortic arch (*left*), left carotid artery (*center*), and left radial artery (*right*). The *p* and *q* waveforms generated by the AdaptModel are indicated by the black curves. The *p* and *q* waveforms generated by the RefModel are indicated by the gray curves. The median *p* and *q* waveforms of the reference waveforms are indicated by the blue dotted curves. The *p* and *q* waveforms generated by the pre adapted model (i.e., with the vessels not adapted) are indicated by the red dashed curves. Systolic, diastolic, and mean pressures are displayed for waveforms generated by the AdaptModel (bold values, black) and the RefModel (ranges, gray) and for the median of all reference waveforms (italic values, blue) and the pre adapted model (red). Root- mean -square errors between adapted and median pressure waveforms, as well as flow waveforms, are described as ϵ_p and ϵ_q, respectively.

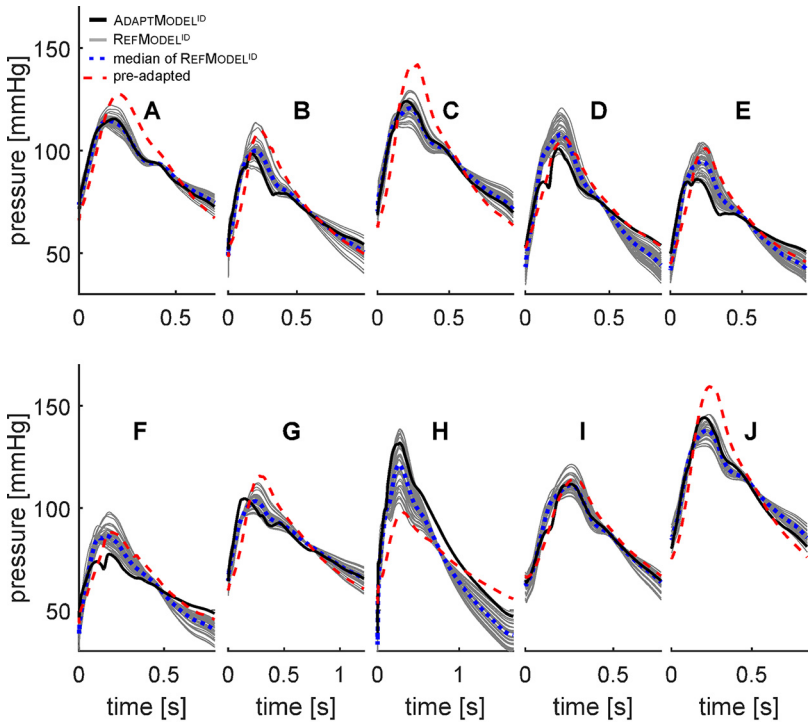

Figure 6. Aortic pressure waveforms for all 10 (i.e., A–J) subjects. Pressure waveforms of the RefModel are indicated by the gray curves. The median pressure waveforms of the reference waveforms are indicated by the blue dotted curves. The pressure waveforms generated by the pre adapted model (i.e., with the vessels not adapted) are indicated by the red dashed curves.

normalization of carotid mean wall shear stress (18). Similarly, chronic decreases in carotid flow, imposed by ligation of the artery, resulted in reductions in carotid diameter (19). The second assumption relates to our model of wall thickness adaptation. We chose to incorporate an additional wall stress component, related to whole body acceleration (Eq. *3*). Our modeling assumption was based on findings from a previous numerical study (20), illustrating the importance of incorporating the effect of whole body acceleration to render physiological wall thickness values for both arteries and veins. Further unraveling the exact mechanism of vascular adaptation, and thus being able to improve our physiological rule, is expected to result in even better estimations of missing data in sparse data sets using our physiology-based methodology.

For all subjects, limits of agreement between model-estimated radius and reference data were in the order of magnitude of 2 mm for radius and 500 μm for wall thickness. The reported reproducibility of the ultrasound-based measurement of dimensions lies between 0.2 and 0.3 mm (28). Furthermore, the theoretical ultrasound resolution for a (7.5 MHz) clinical vascular probe is 0.2 mm. Hence, we submit that our adaptation model yields reasonable estimations for detailed arterial trees as the one considered for this study. Moreover, the head-to-head comparison (Fig. 4 vs. Fig. A4, and Table 3) demonstrated that, overall, the use of the adaptation rules leads to better estimates than the (more economical) simple scaling rules.

In general, agreement between pressure and flow waveforms generated by the AdaptModel and RefModel was adequate for proximal arteries. For example in Fig. 5, root mean square errors, ϵ_p and ϵ_q, were 1.4 to 1.5 mmHg and 0.3 to 7.6 mL·s^{-1}, respectively.

For the distally located arteries, more pronounced differences in pressure and flow waveform shape were observed, especially during diastole (Fig. 5). However, maximal difference in systolic, diastolic, and mean pressure between adapted models and reference data was small. The predicted systolic blood pressure in the ascending aorta was within 1 mmHg of its median reference value (Fig. 5). In the context of studies on noninvasive estimation of systolic central blood pressure, which have reported an agreement of −1.3 ± 3.2 mmHg (bias ± SD, respectively), our method could yield clinically useful estimations of aortic blood pressure (32). Similarly, estimated peak flow rate was in good agreement with reference values (difference in q_{sys} within 10%; Fig. 5). Furthermore, the root mean square errors (ϵ_q, Fig. 5) for flow rate were acceptable in the context of errors found in an in vitro study under steady flow conditions (33). Peak flow rate predictions from PWP models could be used to define boundary conditions in, e.g., aneurysm rupture risk assessment studies using subject-specific computational fluid dynamics (2). In an earlier study, peak wall shear stress was found indicative of aneurysm rupture risk (34).

The variance-based sensitivity analysis, quantifying how model output is influenced by changes in adaptation model

Table 3. *Agreement between estimated and measured radius and wall thickness as determined when applying an adaptation rule or a simple scaling rule*

	Radius, mm		Wall Thickness, μm	
	Bias	2 SD of difference	Bias	2 SD of difference
Adaptation rule	0.2	2.6	−140	557
Simple scaling rule	1.4	3.3	−170	693

parameters, clearly pointed out that adaptation model parameters should be determined for specific applications. For example, mean wall shear stress varies between healthy and diseased subjects, between arteries within the same subject, and also across species (12). In choosing adequate adaptation model parameters, one could use values from earlier reports on measuring mean wall shear stress and wall stress in various species, in various types of patients as well as in different settings (8, 13, 35, 43). Sensitivity analysis indicated that adaptation parameters for radius adaptation (i.e., the target wall shear stress value for proximal arteries) influence the outcome of wall thickness adaptation. This interdependency follows from our formulation of adaptation (Eqs. *2* and *7*) and is based on physiology where wall stress also depends on vessel radius, which in turn is regulated by changes in flow rate (10).

Previous Work on Modeling Vascular Adaptation

Previous studies modeled vascular adaptation through stress growth laws (35) or considered adaptation in extensive growth and remodeling frameworks (36, 37). Such vascular adaptation models often assessed local arterial wall mechanics on the structural level through constitutive equations (26). This allows for constitutive models to resemble a specific artery, for example, the basilar artery as in Valentin et al. (38). Herein, physiologically realistic time courses of elastin-collagen matrix turnover, remodeling, and vascular smooth muscle cell tone in altered flow and intramural pressure situations were obtained (35, 38). In contrast to the aforementioned works, our current implementation of vascular adaptation does not take into account residual stresses, local stress distribution, and constituent-specific stresses. Instead, our implementation of vascular adaptation, relying on only five model parameters (i.e., $\sigma_{f,target}$, $\bar{\tau}_{w,target,prox}$,$\bar{\tau}_{w,target,dist}$, r_{crit}, and v_{impact}) can be considered as a generalization of these more extensive frameworks. Of note, despite our simplified physiological hypotheses in modeling vascular adaptation, we were able to adequately predict vessel geometry and hemodynamics.

Limitations

Comparative evaluation between measured vascular geometries and those estimated by our adaptation model was possible for a sufficiently large number of arterial segments (70 for radius and 20 for wall thickness). Analyses regarding pressure-flow waveforms required input of the geometries of all modeled arteries. To achieve this, we had to calculate scaling factors to gain estimates for arteries that were not measured. Conclusions on the validity of model estimations, especially those containing assumptions regarding geometries of nonmeasured arteries, should be taken with some caution. Therefore, it should be emphasized that the present study does not validate our methodology, but it serves to illustrate the usefulness of our PWP adaptation framework when confronted with incomplete patient-specific data sets.

Our PWP adaption model requires imputation of one carotid arterial diameter and wall thickness value. Both the acquisition technique and the software we used have already been employed in various clinical-epidemiological studies [summarized in Engelen et al. (30)] and are furthermore found to be highly reproducible. We do expect some influence on model predictions in case end users impute data that are noisy or are hampered by measurement uncertainty ("garbage in is garbage out"). However, a possible advantage of using physiology-driven adaptation rules to predict vascular diameter and wall thickness is that such an approach may also help identify unrealistic input data.

Possible Future Developments

Next to mechanical stimuli, metabolic stimuli (e.g., partial oxygen pressure) are known to influence the adaptation of vascular diameter and wall thickness (10, 39). Modeling vascular adaptation based on both mechanical and metabolic drivers has shown to result in the formation of stable microvasculatory networks (40). We expect that incorporation of such metabolic feedback loops into our PWP adaptation framework could benefit its region of applicability, notably when modeling peripheral parts of the circulation in more detail. Extension of our model with rheological properties should be explored in the future studies. An example of a PWP in which non-Newtonian properties were considered was published by Ghigo et al. (41).

It has been suggested that various disease states may alter the adaptive capacity of blood vessels in response to shear stress (e.g., in diabetes mellitus or end-stage renal disease (3, 42–44). Differences between actual blood vessel geometries and those predicted assuming healthy adaptation for these patient groups could provide insight on alterations in or dysfunction of the adaptation mechanism in diseased patients. For future studies, a hypothesis could be that vessels of diabetic patients with disrupted endothelium would have a reduced or dysfunctional response to shear stress.

CONCLUSIONS

We incorporated an adaptation framework based on normalization of wall stress and wall shear stress in blood vessels into a 1-D pulse wave propagation (PWP) model. Our PWP adaptation framework calculates pressures and flows in blood vessels but does not require full parameterization of the arterial domain. Instead, it considers adaptation processes to adequately predict arterial radius (bias ± 2 SD of difference equal to 0.2 ± 2.6 mm) and wall thickness (−140 ± 557 μm). Such an approach could benefit personalized modeling, notably in the case of missing values and sparse data sets as routinely occurs in clinical settings.

ENDNOTE

At the request of the authors, readers are herein alerted to the fact that the source data related to this manuscript may be found at https://doi.org/10.5281/zenodo.4110704. These materials are not a part of this manuscript and have not undergone peer review by the American Physiological Society (APS). APS and the journal editors take no responsibility for these materials, for the Web site address, or for any links to or from it.

GLOSSARY

Symbol	Unit	Meaning
General		
η	Pa s	blood dynamic viscosity
ρ	kg·m^{-3}	blood density
t	s	time
V_r	%	coefficient of variance for tube radius
V_h	%	coefficient of variance for tube wall thickness
PWP model		
α_0	–	characteristic Womersley number
μ	–	Poisson's ratio
δ	–	convection term multiplication factor
ζ_c	–	fraction of lumen area with inertia-dominated flow
A	m^2	vessel lumen cross-sectional area
Awall	m^2	vessel cross-sectional wall area
Cpulse	m·s^{-1}	carotid-to-radial pulse wave velocity
C	m^2·Pa^{-1}	area compliance
Cart	m^3·Pa^{-1}	arterial compliance
D_0	Pa^{-1}	distensibility
E	Pa	Young's modulus
h	m	vessel wall thickness
L	Pa·s^2·m^{-4}	inertance per unit length
p	Pa	transmural pressure
q	m^3·s^{-1}	flow rate
r	m	vessel lumen radius
R_p	Pa·s·m^{-3}	peripheral resistance
z	m	axial vessel coordinate
Z_0	Pa·s·m^{-3}	characteristic impedance
Vascular adaptation		
$\sigma_{f,target}$	Pa	peak wall stress target value
$\tau_{target,prox}$	Pa	wall shear stress target value for proximal arteries
$\tau_{target,distal}$	Pa	wall shear stress target value for distal arteries
k_A	–	wall thickness adaptation feedback factor
k_r	–	radius adaptation feedback factor
r_{crit}	m	critical vessel radius for radius adaptation
v_{impact}	m·s^{-1}	body impact velocity

APPENDIX

Expanded Methods and Results

Blood pressure and tonometry measurements.

Prior to measurements, subjects were rested at least 10 min in the supine position during which oscillometric blood pressure measurements were obtained at the left upper arm (Omron 705IT, Omron Healthcare Europe, The Netherlands). After 10 min, tonometric waveforms were obtained at the brachial, radial, and carotid artery (Sphygmocor, AtCor Medical, Sydney, Australia). The raw arterial tonometry waveforms were used to obtain calibrated local blood pressure waveforms using the method described by Kelly and Fitchett (16). First, the tonometric waveform of the brachial artery (i.e., considered the reference artery) was calibrated using the oscillometric systolic and diastolic blood pressure values. Mean brachial pressure was then calculated as the numerical integral of the calibrated brachial waveform divided by pulse duration. Subsequently, the local pressures of the target arteries (i.e., carotid and radial) were obtained by calibrating tonometric waveforms using diastolic and mean brachial blood pressure assuming the difference between mean pressure and diastolic pressure to remain constant over the arterial tree (16).

Ultrasound Imaging

Ultrasound (US) measurements were performed immediately after tonometry measurements. Diameter measurements were performed at the brachial, radial, ulnar, and carotid artery using an ESAOTE MyLab One (ESAOTE, Maastricht, The Netherlands) scanner equipped with a 4- to 13-MHz linear array probe (SL3323). Diameter waveforms were obtained by means of an RF-based echo wall–tracking tool (RFQAS, ESAOTE, Maastricht, The Netherlands). At the same locations, flow velocity waveforms were obtained by pulsed wave Doppler, with the sample volume set to cover the entire lumen. Carotid artery intima-media thickness was obtained using an automated software tool (RFQIMT, ESAOTE, Maastricht, The Netherlands).

Diameter waveforms and intima-media thickness values were obtained as averages of at least four heart beats. Radial and ulnar flow velocity curves were automatically traced by the US machine, and mean flows were also obtained as averages over 4 to 6 heart beats, by multiplying diastolic lumen area with mean flow velocity.

Both the RFQAS and RFQIMT software are considered reference methods for measuring diameter, distension, and IMT, respectively (45, 46). Previously, our group established reproducibility values of RFQAS-based carotid artery diameter and distension measurements equal to 220 μm for diastolic diameter and 35 μm for distension, respectively (47). In the same study, reproducibility of IMT measurement using RFQIMT was found to be 40 μm.

MR Imaging

An overview of MRI sequence parameters is provided in Table A1. Quantitative flow scans were analyzed using CAAS MR Flow v1.2 (Pie Medical Imaging, Maastricht, Netherlands). By indicating the vessel of interest, vessel contours were automatically detected on all cardiac frames. When necessary, manual adjustments were performed by a cardiologist (B.P.A.) who is trained and experienced in analyzing quantitative MR flow measurements. After accepting all contours, the flow, maximum velocity, minimum velocity, mean velocity, and vessel area were calculated per cardiac phase and per flow-encoding direction. The net flow and net maximum velocity of each vessel were calculated using the data of all three flow-encoding directions. Black blood vessel wall images were analyzed using CAAS MR Viewer v4.3.

Pulse Wave Propagation Model

We modeled blood vessels as linear thick-walled elastic tubes. Blood was assumed to be incompressible and Newtonian. Furthermore, gravity forces and leakage along

the length of the tube were neglected. Applying conservation of mass and the momentum equations, and integrating over the vessel's cross section, yield the governing equations (24, 30):

$$C\frac{\partial p}{\partial t}+\frac{\partial q}{\partial z}=0, \tag{A1}$$

$$\frac{\rho}{A}\left(\frac{\partial q}{\partial t}+\frac{\partial \gamma}{\partial z}\right)+\frac{\partial p}{\partial z}=\frac{2}{r}\tau_w. \tag{A2}$$

where $p=p(z,t)$ is the pressure, $q=q(z,t)$ is the flow rate, $A=A(z,t)$ is the cross-sectional lumen area, and z is the axial vessel distance. The parameter $C=C(z)$ denotes the vessels' area compliance, constant ρ is the blood density, and r is the radius using $r(z,t)=\sqrt{A/\pi}$. Variable τ_w denotes wall shear stress, and $\frac{\rho}{A}\frac{\partial \gamma}{\partial z}$ denotes the convection term, with γ being the axial blood velocity (v_z) squared integrated over the cross-sectional area, i.e., $\gamma=\int_A v_z^2 dA$. To be able to solve the above equations, we need a good approximation for τ_w and $\frac{\partial \gamma}{\partial z}$ in terms of p and q in combination with a constitutive law between A and p. For this purpose, we used the approximate velocity profile, introduced earlier (48) that approximates the Womersley profile in the time domain. The wall shear stress is then given by

$$\tau_w=\frac{2\eta}{(1-\zeta_c)r}\frac{q}{A}+\frac{r}{4}(1-\zeta_c)\frac{\partial p}{\partial z}, \tag{A3}$$

with $\zeta_c=\left(\max\left[0,1-\frac{\sqrt{2}}{\alpha_0}\right]^2\right)$. Constant η is the dynamic blood viscosity, ζ_c is the fraction of cross-sectional area with inertia-dominated flow, and α is the characteristic Womersley number, given by $\alpha_0=\sqrt{\frac{2A_0\rho}{T\eta}}$. Here, A_0 denotes reference area, p_0 the reference pressure, and T the cardiac cycle duration. For two limiting cases, given by $\alpha_0\ll\sqrt{2}$ and $\alpha_0\gg\sqrt{2}$, we obtain $\zeta_c\approx 0$, describing a Poiseuille profile and $\zeta_c\approx 1$, describing a flat velocity profile. Using the approximate velocity profile, $\frac{\partial \gamma}{\partial z}$ is estimated by $\frac{\partial}{\partial z}\left(\delta\frac{q^2}{A}\right)$. The expression for factor δ is given by (48)

$$\delta=\frac{2-2\zeta_c(1-\ln(\zeta_c))}{(1-\zeta_c)^2}. \tag{A4}$$

In this study, compliance was assumed linear around reference pressure, p_0 (i.e., $C\approx C_0=\frac{\partial A}{\partial p}|_{p=p_0}$). For a thick-walled elastic tube, an expression for C_0 was mathematically derived by Jager (49) and applied by Westerhof et al. (50):

$$C_0=\frac{2\pi r_0^2\left(\frac{2r_0^2(1-\mu^2)}{h_0^2}+(1+\mu)\left(\frac{2r_0}{h_0}+1\right)\right)}{E\left(\frac{2r_0}{h_0}+1\right)}. \tag{A5}$$

Constant μ is Poisson's ratio, E is Young's modulus, and r_0 and h_0 denote reference radius and wall thickness, respectively. The area change as a function of pressure can be estimated as

$$A(z,t)=A_0+C_0(p-p_0), \tag{A6}$$

when assuming small pressure changes with respect to the reference pressure and a linearized (constant) area compliance.

Governing Equation for the Periphery

The contribution of the peripheral vasculature at each arterial terminus was lumped in a three-element Windkessel model (Fig. A1). Characteristic impedance (Z_0) represents the lossless wave impedance at the entrance of a peripheral vascular bed. Peripheral resistance (R_p) represents total resistance of a peripheral vascular bed, and peripheral compliance (C_{art}) represents total compliance of a peripheral vascular bed. We chose Z_0 of peripheral vascular beds that terminate the brachiocephalic artery, carotid artery, and the thoracic aorta, equal to $\sqrt{L/C}$, with L and C, respectively, the inertia and compliance at the terminal node of the arterial segment. This was chosen to avoid nonphysiological reflections at high frequencies (i.e., >3 times the heart frequency). Pressure at the end of the Windkessel was kept at 0 mmHg. Furthermore, extravascular pressure of tubes was kept at 0 mmHg. Windkessel resistance (R_p) and compliance (C_{art}) were based on the subject-specific flow distribution to each arterial branch, determined using a method described earlier (51).

The differential equation governing the relation between pressure and flow is given by Reymond et al. (15):

$$\frac{\partial q}{\partial t}=\frac{1}{Z_0}\frac{\partial p}{\partial t}+\frac{p}{Z_0R_pC_{art}}-\left(1+\frac{Z_0}{R_p}\right)\frac{q}{Z_0C_{art}}. \tag{A7}$$

Previous works chose distal Z_0 based on a fixed fraction of R_p or used a single resistor to terminate small arterial branches (15, 52). Here, we explicitly assumed $Z_0\ll R_p$ by fixing Z_0 at 10^{-2} Pa s m^{-3} for peripheral elements terminating the vertebral, radial, ulnar, and interosseous artery (53).

Numerical Implementation of the PWP-Adaptation Framework

Coupling and solving of 1-D mass conservation and momentum balance equations (i.e., *Eqs. A1* and *A2*) and the 0-D equation for pressure and flow in the periphery (Eq. *A7*) was performed using a previously published method (14). We used a simplified trapezoidal scheme for spatial discretization. The second-order backward difference scheme was used for time discretization. We chose an element size (i.e., Δz, indicating the distance between nodes) of 0.01 m, as this resulted in adequate numerical convergence (14). A schematic overview of the PWP adaptation framework is shown in Fig. A2.

Nodal pressures were solved for globally and nodal flows were subsequently computed from the pressures on element level (Fig. A2). The method used for solving the system of 0-D and 1-D equations has been tested earlier in a benchmark study, showing reliable results (54). Convergence of the calculated hemodynamics was evaluated after each simulated cardiac cycle. Hereto, the calculated nodal pressures, $p(t)$, of the current cycle (n) were compared with those of the previous cycle ($n-1$). An expression for the hemodynamic convergence norm (ε) is given as a relative root mean square:

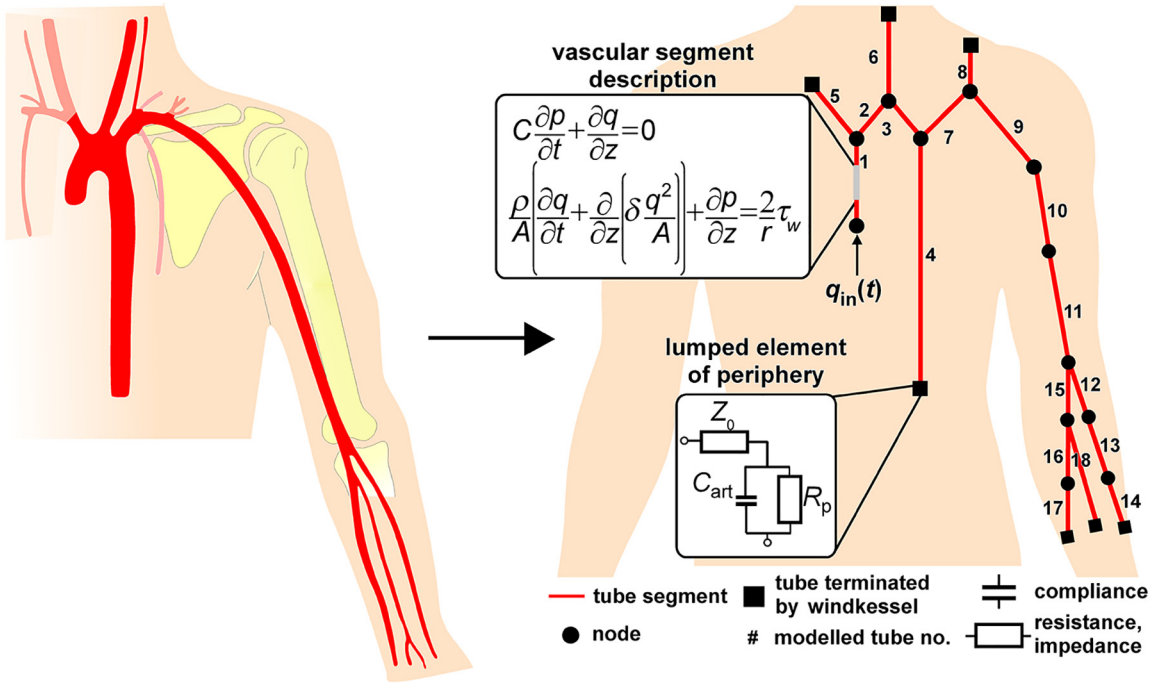

Figure A1. Overview of modeled domain describing the arteries of the aorta and carotid, and the arteries of the left arm. Generic tube properties can be retrieved from Table A2.

$$\epsilon = \max_i \left(\sqrt{\frac{\sum_{t=0}^{T} \left(p_{i,n}^t - p_{i,n-1}^t\right)^2}{\sum_{t=0}^{T} \left(p_{i,n-1}^t\right)^2}} \right), \qquad (A8)$$

where i is the nodal point number. Following hemodynamic convergence, arterial radius and wall thickness of nodes were adapted based on the adaptation rules. For the next cycle ($n = n + 1$), it was evaluated whether ε was still below the convergence criterion and whether the model-estimated wall stress and mean wall shear stress had converged to their respective target values (Fig. A2). Adaptation convergence was evaluated by calculating the relative error of wall stress and wall shear stress given by

$$\epsilon_a(\bullet) = \max(|\bullet - 1|), \qquad (A9)$$

with $(\bullet) = \left\{\frac{\sigma_{f,N,i}}{\sigma_{f,max}}, \frac{\bar{\tau}_{w,N,i}}{\bar{\tau}_{w,target}}\right\}$. Here, $\sigma_{f,N,i}$ and $\bar{\tau}_{w,N,i}$ denote the wall stress and mean wall shear stress values for tube N, respectively. We kept the hemodynamics and adaptation convergence criteria at 10^{-3} to ensure complete adaptation. In Fig. A3, a representative example of adaptation of tube radius and wall thickness is shown.

Since we were interested in only the adapted geometries and not in the adaptation time course, feedback factors k_A and k_r were kept at 0.10 to ensure on the one hand numerical

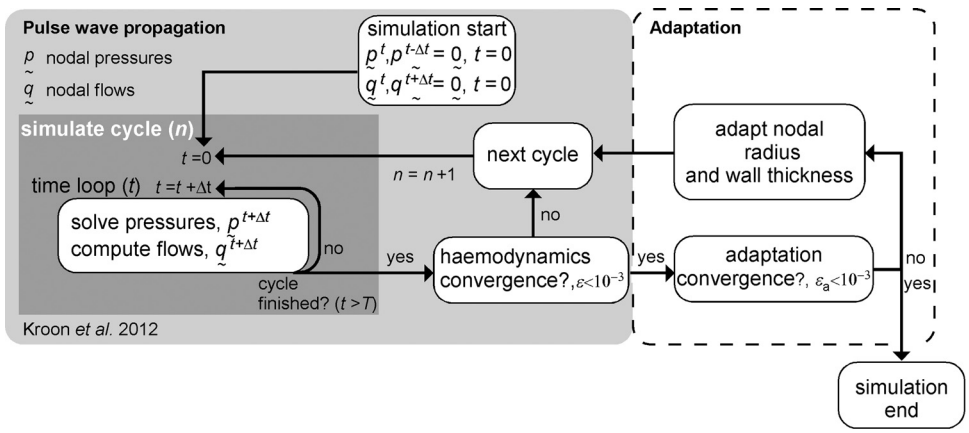

Figure A2. Schematic overview of the PWP adaptation framework. We used a time loop for simulating a single cardiac cycle with cycle duration T and time step Δt. The time loop was continued until hemodynamics convergence (defined as $\epsilon < 10^{-3}$) was achieved, indicating a steady-state simulation. Upon hemodynamic convergence, adaptation convergence was evaluated (i.e., $\epsilon_a < 10^{-3}$). Nodal radius and wall thickness were adapted until adaptation convergence was achieved, indicating normalization of wall stress and wall shear stress to target values.

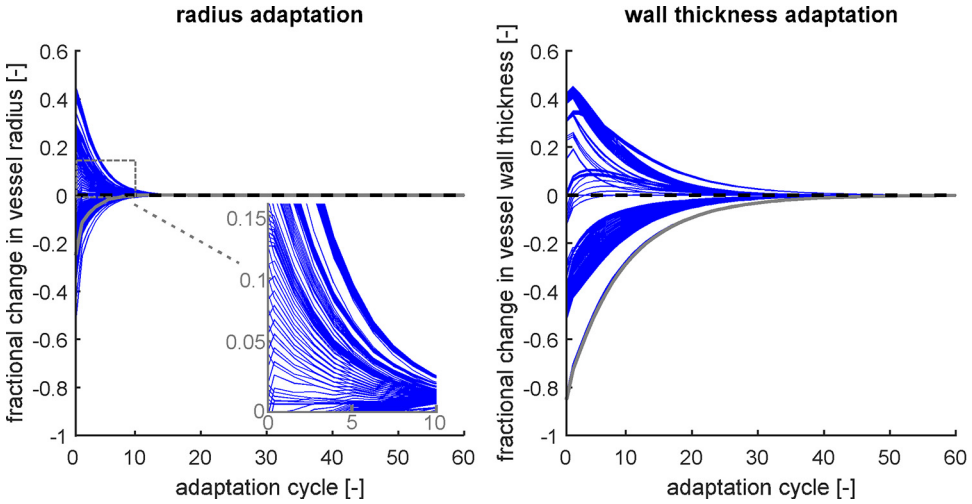

Figure A3. Adaptation of vessel radius (*left*) and wall thickness (*right*) for all modeled vascular segments. The fractional change of vessel radius and wall thickness is plotted as a function of the number of adaptat-ion cycles following departure from generic values. The gray curve for vessel radius and wall thickness highlights the adaptation behavior of a randomly chosen vascular segment.

stability and to reduce on the other hand computational cost. Correspondingly, adaptation convergence was reached after ~50 cycles.

We performed all model simulations and processing steps using MATLAB 2015a (The MathWorks, Natick, MA). For all simulations, the time step (Δt) was kept at 1 ms. Following previous studies, density of blood (ρ) was chosen at 1050 kg m^{-3}, dynamic blood viscosity (η) was chosen at 3×10^{-3} Pa s, and Poisson's ratio (μ) was chosen at 0.5, indicating incompressibility of the vessel wall (14, 50).

Uniqueness of Predicted Geometries

First, to evaluate whether radius and wall thickness adaptation resulted in unique vessel geometries, 10 sets of initial vessel geometries were randomly generated. Random vessel geometries were generated by multiplying the generic vessel geometries (Table A2) with random values, obtained using MATLAB's normal random number generator (i.e., `normrnd(mu,sd)`, with mu = 1.0 and sd = 0.15, respectively). To assess uniqueness, two coefficients of variation for tube radius and wall thickness were calculated (i.e., $V_r = \sigma_r/\mu_r \times 100\%$ and $V_h = \sigma_h/\mu_h \times 100\%$). Here, σ_r and σ_h denote, respectively, the standard deviation of the adapted tube radii and wall thicknesses and μ_r and μ_h denote mean take-off values.

Pressure and Flow Waveforms

Second, we compared pressure and flow waveforms generated by the AdaptModel to waveforms generated by the RefModel. Since the reference data used for the RefModel itself are hampered by measurement error, an envelope of realizations of reference PWP models was obtained, based on assumed measurement errors of ±10% for radius and ±40% for wall thickness (55). Using Latin hypercube sampling, a total of 40 samples of reference radius and wall thickness were drawn and incorporated into the RefModel (56).

Sensitivity Analysis of Adaptation Model Parameters

Third, a variance-based sensitivity analysis (57) was performed to assess how pressure waveform characteristics and the errors in radius and wall thickness estimations changed when varying adaptation model parameters. Adaptation model parameters (i.e., $\sigma_{f,target}$, $\bar{\tau}_{w,target,prox}$, $\bar{\tau}_{w,target,dist}$, $r_{crit,}$ and v_{impact}) varied between ±50% of their initial value. In total, 241 combinations of adaptation model parameter simulations were evaluated.

We then selected the following characteristics to assess sensitivity to adaptation model parameter variance:

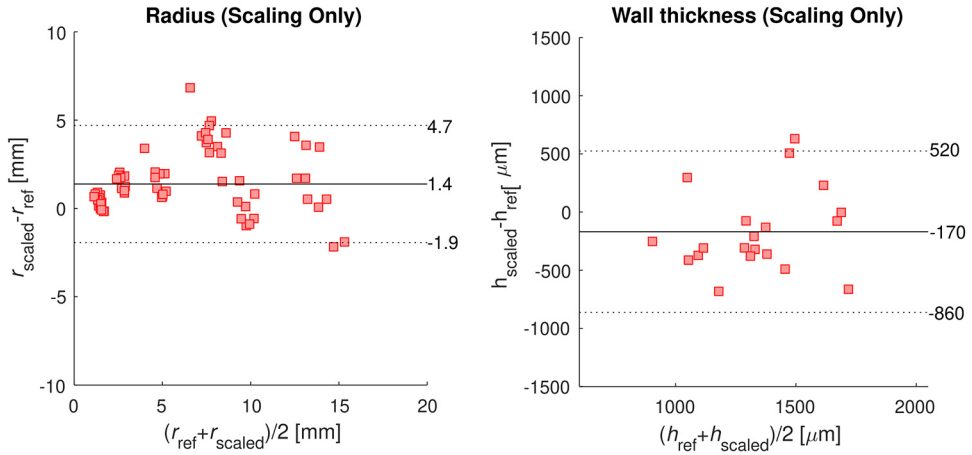

Figure A4. Bland–Altman plots of agreement between simple scaling rule approach ("scaling only") and measured radius (*r*) and wall thickness (*h*). Values on right side of each plot indicate bias and limits of agreement.

Table A1. *MRI sequence parameters*

	3-D TFE Aortic Arch	2-D TFE Quantitative Flow	2-D TSE BB Vessel Wall
Echo time, ms	1.0	2.2	60
Repetition time, ms	3.3	3.8	2 beats
Flip angle,°	20	10	90
Field of view, mm	320 × 280 × 120	350 × 300	350 × 350
Slice thickness, mm	-	8	8
Acquired resolution, mm	2.0 × 2.0 × 3.0	2.5 × 2.5	1.40 × 1.75
Reconstructed resolution, mm	1.0 × 1.0 × 1.5	1.2 × 1.2	0.88 × 0.88

- Aortic systolic and diastolic pressure ($p_{s,aorta}$ and $p_{d,aorta}$, respectively)
- Radial systolic and diastolic pressure ($p_{s,radial}$ and $p_{d,radial}$, respectively)
- Pulse pressure amplification (Δp_{amp})
- Carotid-to-radial pulse wave velocity (c_{pulse})
- The root mean square error for the estimation of tube radius (ϵ_r)
- The root mean square error for tube wall thickness (ϵ_h)

Output Δp_{amp} was defined as the ratio between radial pulse pressure and aortic pulse pressure, according to established methods (58). Output c_{pulse} was obtained by dividing the path length between the terminal nodes of the tubes that modeled the carotid artery and radial artery by the pulse transit time between these nodes.

The adaptive sparse grid polynomial chaos expansion (agPCE) method (57) can assess parameter sensitivity using an adaptively constructed finite polynomial expansion *f*agPCE:

$$X_i = f^{X_i}(\mathbf{M}) \approx f^{X_i}_{agpce}(\mathbf{M}). \quad (A10)$$

Here, $\mathbf{X}$ contains the above-mentioned output characteristics. Furthermore, $\mathbf{M}$ contains adaptation model parameters.

From the metamodel, the variance of an output characteristic (a measure of its uncertainty) can be derived analytically. In addition, the following sensitivity metrics were computed from the metamodel:

- Main sensitivity indices: The main sensitivity index (S_i) of adaptation model parameter M_i represents the expected reduction in uncertainty of the output characteristic if M_i were known exactly. Assessment of S_i determines which measured variables are most rewarding to be measured more accurately to reduce model output uncertainty (i.e., parameter prioritization) (29).
- Total sensitivity indices: The total sensitivity index (S_T) of M_i represents the expected uncertainty in the output characteristic that would remain if all other adaptation model parameters except M_i were known exactly. Assessment of S_T determines which measured variables could potentially be fixed within their uncertainty domain (i.e., parameter fixing) (29).

The quality of the metamodel from which sensitivities were derived can be expressed using the leave-one-out cross-validation coefficient (Q^2). Adequate metamodel construction was ensured by enforcing a Q^2 of at least 0.990.

GRANTS

This study was supported by a Kootstra Talent Fellowship from Maastricht University Medical Center (to M. H. G. Heuskinkveld) and Stichting De Weijerhorst (to R. J. Holtackers and B. P. Adriaans).

DISCLOSURES

No conflicts of interest, financial or otherwise, are declared by the authors.

Table A2. Generic values of modeled arterial segments (5, 15)

Tube	Arterial Segment	*l*, cm	$r_{proximal}$, mm	r_{distal}, mm	*h*, mm	*E* (105 Pa)	$\bar{q}$, mL/min
1	Ascending aorta	4.00	14.70	14.70	1.47	4.0	5.2×10^3
2	Aortic arch A proximal	2.00	12.60	12.00	1.23	4.0	
3	Aortic arch A distal	3.90	10.70	10.40	1.06	4.0	
4	Aortic arch B + thoracic aorta	15.60	10.00	6.50	1.91	4.0	4.2×10^3
5	Brachiocephalic	3.40	10.10	9.00	0.82	4.0	470
6	Left carotid	9.10	6.80	3.50	0.51	4.0	360
7	Left subclavian	3.40	5.80	4.50	0.51	4.0	
8	Left vertebral	14.90	1.90	0.90	0.21	8.0	26
9	Left subclavian + axillary. + brachial proximal	14.77	4.10	3.60	0.57	4.0	
10	Left brachial middle	14.77	3.60	3.10	0.50	4.0	
11	Left brachial distal	14.77	3.10	2.40	0.55	4.0	
12	Left radial proximal	7.83	1.90	1.80	0.36	8.0	
13	Left radial middle	7.83	1.80	1.70	0.34	8.0	
14	Left radial distal	7.83	1.70	1.60	0.32	8.0	40
15	Left ulnar proximal	6.70	1.90	1.70	0.36	8.0	
16	Left ulnar middle	7.90	1.60	1.50	0.31	8.0	
17	Left ulnar distal	8.55	1.50	1.40	0.29	8.0	30
18	Left interosseous	8.55	1.10	0.90	0.20	16.0	30

l, length of the arterial segment; $r_{proximal}$, proximal radius; r_{distal}, distal radius; *h*, wall thickness; and *E*, Young's modulus. Mean flow rate $\bar{q}$ represents either the proximal inflow or the terminal flow assigned to the peripheral elements of the model.

Table A3. *Main (S_i) and total (S_T) sensitivities of selected hemodynamic characteristics and estimated geometries to adaptation parameters.*

	$\bar{\tau}_{w,\text{target,prox}}$		$\bar{\tau}_{w,\text{target,dist}}$		r_{crit}		$\sigma_{f,\text{target}}$		v_{impact}			
	S_i	S_T	S_i	S_T	S_i	S_T	S_i	S_T	S_i	S_T	Var (X)	Q^2
$p_{s,aorta}$, mmHg	0.77	0.95	0	0	0.054	0.23	0	0	0	0	59.52 mmHg^2	0.99998
$p_{d,aorta}$, mmHg	0.99	0.99	0	0	0	0	0	0	0	0	52.89 mmHg^2	0.99957
$p_{s,radial}$, mmHg	0.97	0.99	0	0	0.0081	0.028	0	0	0	0	261.48 mmHg^2	0.99983
$p_{d,radial}$, mmHg	0.96	0.99	0	0	0.014	0.04	0	0	0	0	39.83 mmHg^2	0.99998
c_{pulse}, m s^{-1}	0.41	0.82	0.18	0.59	0	0	0	0	0	0	0.24 (m s^{-1})^2	0.99986
Δp_{amp} (-)	0.075	0.77	0	0	0.23	0.92	0	0	0	0	0.027	0.99978
ε_r, µm	0.99	0.99	0	0	0	0	0	0	0	0	0.126 m^2	0.99979
ε_h, µm	0.016	0.06	0	0	0	0	0.51	0.88	0.097	0.43	0.0169 m^2	0.99463

Q^2, leave-one-out cross-validation coefficient; VAR(X), variance of the pressure waveform parameters as present in the simulations of the sensitivity analysis.

AUTHOR CONTRIBUTIONS

M.H.G.H., R.J.H., T.A., T.D., K.D.R., and W.H. conceived and designed research; M.H.H., R.J.H., and J.O. performed experiments; M.H.G.H., R.J.H., B.P.A., T.D., K.D.R., and W.H. analyzed data; M.H.H., R.J.H., B.P.A., T.A., T.D., K.D.R., and W.H. interpreted results of experiments; M.H.G.H. prepared figures; M.H.G.H. drafted manuscript; M.H.G.H., R.J.H., B.P.A., T.A., T.D., K.D.R., and W.H. edited and revised manuscript; R.J.H., B.P.A., J.O., T.A., T.D., K.D.R., and W.H. approved final version of manuscript.

REFERENCES

1. **Hughes TJ**, **Lubliner J.** On the one-dimensional theory of blood flow in the larger vessels. *Math Biosci* 18: 161–170, 1973. doi:10.1016/0025-5564(73)90027-8.
2. **van de Vosse FN**, **Stergiopulos N.** Pulse wave propagation in the arterial tree. *Annu Rev Fluid Mech* 43: 467–499, 2011. doi:10.1146/annurev-fluid-122109-160730.
3. **Caroli A**, **Manini S**, **Antiga L**, **Passera K**, **Ene-Iordache B**, **Rota S**, **Remuzzi G**, **Bode A**, **Leermakers J**, **van de Vosse FN**, **Vanholder R**, **Malovrh M**, **Tordoir J**, **Remuzzi A**; **ARCH project Consortium.** Validation of a patient-specific hemodynamic computational model for surgical planning of vascular access in hemodialysis patients. *Kidney Int* 84: 1237–1245, 2013. doi:10.1038/ki.2013.188.
4. **Driessen RS**, **Danad I**, **Stuijfzand WJ**, **Raijmakers PG**, **Schumacher SP**, **van Diemen PA**, **Leipsic JA**, **Knuuti J**, **Underwood SR**, **van de Ven PM**, **van Rossum AC**, **Taylor CA**, **Knaapen P.** Comparison of coronary computed tomography angiography, fractional flow reserve, and perfusion imaging for ischemia diagnosis. *J Am Coll Cardiol* 73: 161–173, 2019. doi:10.1016/j.jacc.2018.10.056.
5. **Huberts W**, **Bode AS**, **Kroon W**, **Planken RN**, **Tordoir JH**, **van de Vosse FN**, **Bosboom EM.** A pulse wave propagation model to support decision-making in vascular access planning in the clinic. *Med Eng Phys* 34: 233–248, 2012. doi:10.1016/j.medengphy.2011.07.015.
6. **Zonnebeld N**, **Huberts W**, **van Loon MM**, **Delhaas T**, **Tordoir JHM.** Preoperative computer simulation for planning of vascular access surgery in hemodialysis patients. *J Vasc Access* 18: 118–124, 2017. doi:10.5301/jva.5000661.
7. **Huberts W**, **Donders WP**, **Delhaas T**, **van de Vosse , FN.** Applicability of the polynomial chaos expansion method for personalization of a cardiovascular pulse wave propagation model. *Int J Numer Meth Biomed Eng* 31: e02720, 2015 [Erratum in *Int J Numer Method Biomed Eng* 30:1679–1704]. doi:10.1002/cnm.2720.
8. **Epstein S**, **Willemet M**, **Chowienczyk PJ**, **Alastruey J.** Reducing the number of parameters in 1D arterial blood flow modeling: less is more for patient-specific simulations. *Am J Physiol Heart Circ Physiol* 309: H222–H234, 2015. doi:10.1152/ajpheart.00857.2014.
9. **Wolinsky H.** Long-term effects of hypertension on the rat aortic wall and their relation to concurrent aging changes: morphological and chemical studies. *Circ Res* 30: 301–309, 1972. doi:10.1161/01.res.30.3.301.
10. **Humphrey JD.** Vascular adaptation and mechanical homeostasis at tissue, cellular, and sub-cellular levels. *Cell Biochem Biophys* 50: 53–78, 2008. doi:10.1007/s12013-007-9002-3.
11. **Matsumoto T**, **Hayashi K.** Stress and strain distribution in hypertensive and normotensive rat aorta considering residual strain. *J Biomech Eng* 118: 62–73, 1996. doi:10.1115/1.2795947.
12. **Reneman RS**, **Hoeks AP.** Wall shear stress as measured in vivo: consequences for the design of the arterial system. *Med Biol Eng Comput* 46: 499–507, 2008. doi:10.1007/s11517-008-0330-2.
13. **Glagov S**, **Zarins C**, **Giddens DP**, **Ku D.** Hemodynamics and atherosclerosis. Insights and perspectives gained from studies of human arteries. *Arch Pathol Lab Med* 112: 1018–1031, 1988.
14. **Kroon W**, **Huberts W**, **Bosboom M**, **van de Vosse F.** A numerical method of reduced complexity for simulating vascular hemodynamics using coupled 0D lumped and 1D wave propagation models. *Comput Math Methods Med* 2012: 156094, 2012. doi:10.1155/2012/156094.
15. **Reymond P**, **Merenda F**, **Perren F**, **Rüfenacht D**, **Stergiopulos N.** Validation of a one-dimensional model of the systemic arterial tree. *Am J Physiol Heart Circ Physiol* 297: H208–H222, 2009. doi:10.1152/ajpheart.00037.2009.
16. **Kelly R**, **Fitchett D.** Noninvasive determination of aortic input impedance and external left ventricular power output: a validation and repeatability study of a new technique. *J Am Coll Cardiol* 20: 952–963, 1992. doi:10.1016/0735-1097(92)90198-V.
17. **Leguy CA**, **Bosboom EM**, **Gelderblom H**, **Hoeks AP**, **van De Vosse F.** Estimation of distributed arterial mechanical properties using a wave propagation model in a reverse way. *Med Eng Phys* 32: 957–967, 2010. doi:10.1016/j.medengphy.2010.06.010.
18. **Kamiya A**, **Togawa T.** Adaptive regulation of wall shear stress to flow change in the canine carotid artery. *Am J Physiol Heart Circ Physiol* 239: H14–H21, 1980. doi:10.1152/ajpheart.1980.239.1.H14.
19. **Langille B**, **O'Donnell F.** Reductions in arterial diameter produced by chronic decreases in blood flow are endothelium-dependent. *Science* 231: 405–407, 1986. doi:10.1126/science.3941904.
20. **Arts T**, **Reesink K**, **Kroon W**, **Delhaas T.** Simulation of adaptation of blood vessel geometry to flow and pressure: Implications for arteriovenous impedance. *Mech Res Commun* 42: 15–21, 2012. doi:10.1016/j.mechrescom.2011.10.005.
21. **Mattson JM**, **Zhang , Y.** Structural and functional differences between porcine aorta and vena cava. *J Biomech Eng* 139: 0710071–0710078, 2017. doi:10.1115/1.4036261.
22. **Arts T**, **Delhaas T**, **Bovendeerd P**, **Verbeek X**, **Prinzen FW.** Adaptation to mechanical load determines shape and properties of heart and circulation: the CircAdapt model. *Am J Physiol Heart Circ Physiol* 288: H1943–H1954, 2005. doi:10.1152/ajpheart.00444.2004.
23. **Anderson FC**, **Pandy MG.** Storage and utilization of elastic strain energy during jumping. *J Biomech* 26: 1413–1427, 1993. doi:10.1016/0021-9290(93)90092-s.
24. **Reneman RS**, **Arts T**, **Hoeks AP.** Wall shear stress–an important determinant of endothelial cell function and structure–in the arterial system in vivo. Discrepancies with theory. *J Vasc Res* 43: 251–269, 2006. doi:10.1159/000091648.
25. **Miller BG**, **Gattone VH 2nd**, **Overhage JM**, **Bohlen HG**, **Evan AP.** Morphological evaluation of vascular smooth muscle cell: length and

width from a single scanning electron micrograph of microvessels. *Anat Rec* 216: 95–103, 1986. doi:10.1002/ar.1092160116.
26. **Caro CG.** *The Mechanics of the Circulation* (2nd ed.). London: Cambridge University Press, 2012. https://doi.org/10.1017/CBO9781139013406.
27. **Taylor CA**, **Cheng CP**, **Espinosa LA**, **Tang BT**, **Parker D**, **Herfkens RJ.** In vivo quantification of blood flow and wall shear stress in the human abdominal aorta during lower limb exercise. *Ann Biomed Eng* 30: 402–408, 2002. doi:10.1114/1.1476016.
28. **Dammers R**, **Tordoir JH**, **Hameleers JM**, **Kitslaar PJ**, **Hoeks AP.** Brachial artery shear stress is independent of gender or age and does not modify vessel wall mechanical properties. *Ultrasound Med Biol* 28: 1015–1022, 2002. doi:10.1016/S0301-5629(02)00544-6.
29. **Saltelli A**, **Ratto M**, **Andres T**, **Campolongo F**, **Cariboni J**, **Gatelli DSM**, **Tarantola S.** *Global Sensitivity Analysis: The Primer*. Hoboken, NJ: John Wiley & Sons, 2008.
30. **Engelen L**, **Bossuyt J**, **Ferreira I**, **van Bortel LM**, **Reesink KD**, **Segers P**, **Stehouwer CD**, **Laurent S**, **Boutouyrie P**; **Reference values for Arterial Measurements Collaboration.** Reference values for local arterial stiffness. Part A: carotid artery. *J Hypertens* 33: 1981–1996, 2015. doi:10.1097/HJH.0000000000000654.
31. **van den Munckhof ICL**, **Jones H**, **Hopman MTE**, **de Graaf J**, **Nyakayiru J**, **van Dijk B**, **Eijsvogels TMH**, **Thijssen DHJ.** Relation between age and carotid artery intima-medial thickness: a systematic review. *Clin Cardiol* 41: 698–704, 2018. doi:10.1002/clc.22934.
32. **Sharman JE**, **Lim R**, **Qasem AM**, **Coombes JS**, **Burgess MI**, **Franco J**, **Garrahy P**, **Wilkinson IB**, **Marwick TH.** Validation of a generalized transfer function to noninvasively derive central blood pressure during exercise. *Hypertension* 47: 1203–1208, 2006. doi:10.1161/01.HYP.0000223013.60612.72.
33. **Hoyt K**, **Hester FA**, **Bell RL**, **Lockhart ME**, **Robbin ML.** Accuracy of volumetric flow rate measurements: an in vitro study using modern ultrasound scanners. *J Ultrasound Med* 28: 1511–1518, 2009. doi:10.7863/jum.2009.28.11.1511.
34. **Castro M**, **Putman C**, **Radaelli A**, **Frangi A**, **Cebral J.** Hemodynamics and rupture of terminal cerebral aneurysms. *Acad Radiol* 16: 1201–1207, 2009. doi:10.1016/j.acra.2009.03.022.
35. **Rachev A.** A model of arterial adaptation to alterations in blood flow. *J Elast* 61: 83–111, 2000. doi:10.1023/A:1010800703478.
36. **Humphrey J**, **Rajagopal K.** A constrained mixture model for growth and remodeling of soft tissues. *Math Models Methods Appl Sci* 12: 407–430, 2002. doi:10.1142/S0218202502001714.
37. **Rodriguez EK**, **Hoger A**, **McCulloch AD.** Stress-dependent finite growth in soft elastic tissues. *J Biomech* 27: 455–467, 1994. doi:10.1016/0021-9290(94)90021-3.
38. **Valentin A**, **Cardamone L**, **Baek S**, **Humphrey JD.** Complementary vasoactivity and matrix remodelling in arterial adaptations to altered flow and pressure. *J R Soc Interface* 6: 293–306, 2009. doi:10.1098/rsif.2008.0254.
39. **Zakrzewicz A**, **Secomb TW**, **Pries AR.** Angioadaptation: keeping the vascular system in shape. *Physiology* 17: 197–201, 2002. doi:10.1152/nips.01395.2001.
40. **Pries AR**, **Secomb TW.** Modeling structural adaptation of microcirculation. *Microcirculation* 15: 753–764, 2008. doi:10.1080/10739680802229076.
41. **Ghigo A**, **Lagrée PY**, **Fullana , JM.** A time-dependent non-Newtonian extension of a 1D blood flow model. *J Nonnewton Fluid Mech* 253: 36–49, 2018. doi:10.1016/j.jnnfm.2018.01.004.
42. **Cooper ME**, **Bonnet F**, **Oldfield M**, **Jandeleit-Dahm K.** Mechanisms of diabetic vasculopathy: an overview. *Am J Hypertens* 14: 475–486, 2001. doi:10.1016/s0895-7061(00)01323-6.
43. **Dammers R**, **Tordoir JH**, **Kooman JP**, **Welten RJ**, **Hameleers JM**, **Kitslaar PJ**, **Hoeks AP.** The effect of flow changes on the arterial system proximal to an arteriovenous fistula for hemodialysis. *Ultrasound Med Biol* 31: 1327–1333, 2005. doi:10.1016/j.ultrasmedbio.2005.03.017.
44. **Ene-Iordache B**, **Mosconi L**, **Antiga L**, **Bruno S**, **Anghileri A**, **Remuzzi G**, **Remuzzi A.** Radial artery remodeling in response to shear stress increase within arteriovenous fistula for hemodialysis access. *Endothelium* 10: 95–102, 2003. doi:10.1080/10623320303365.
45. **Brands PJ**, **Hoeks AP**, **Willigers J**, **Willekes C**, **Reneman RS.** An integrated system for the non-invasive assessment of vessel wall and hemodynamic properties of large arteries by means of ultrasound. *Eur J Ultrasound* 9: 257–266, 1999. doi:10.1016/S0929-8266(99)00033-6.
46. **Willekes C**, **Hoeks AP**, **Bots ML**, **Brands PJ**, **Willigers JM**, **Reneman RS.** Evaluation of off-line automated intima–media thickness detection of the common carotid artery based on M-line signal processing. *Ultrasound Med Biol* 25: 57–64, 1999. doi:10.1016/S0301-5629(98)00138-0.
47. **Holtackers RJ**, **Spronck B**, **Heusinkveld MH**, **Crombag G**, **Op t'Roodt J**, **Delhaas T**, **Kooi ME**, **Reesink KD**, **Hermeling E.** Head orientation should be considered in ultrasound studies on carotid artery distensibility. *J Hypertens* 34: 1551–1555, 2016. doi:10.1097/HJH.0000000000000985.
48. **Bessems D**, **Rutten M**, **Van De Vosse , F.** A wave propagation model of blood flow in large vessels using an approximate velocity profile function. *J Fluid Mech* 580: 145–168, 2007. doi:10.1017/S0022112007005344.
49. **Jager G.** *Electrical Model of the Human Arterial Tree* (PhD thesis). Utrecht, The Netherlands: Utrecht University, 1965.
50. **Westerhof N**, **Bosman F**, **De Vries CJ**, **Noordergraaf A.** Analog studies of the human systemic arterial tree. *J Biomech* 2: 121–143, 1969. doi:10.1016/0021-9290(69)90024-4.
51. **Mulder G**, **Bogaerds AC**, **Rongen P**, **van de Vosse FN.** The influence of contrast agent injection on physiological flow in the circle of Willis. *Med Eng Phys* 33: 195–203, 2011. doi:10.1016/j.medengphy.2010.09.021.
52. **Watanabe SM**, **Blanco PJ**, **Feijóo RA.** Mathematical model of blood flow in an anatomically detailed arterial network of the arm. *Esaim Math Model Numer Anal* 47: 961–985, 2013. doi:10.1051/m2an/2012053.
53. **Alastruey J**, **Moore S**, **Parker K**, **David T**, **Peiró J**, **Sherwin S.** Reduced modelling of blood flow in the cerebral circulation: coupling 1-D, 0-D and cerebral autoregulation models. *Int J Numer Meth Fluids* 56: 1061–1067, 2008. doi:10.1002/fld.1606.
54. **Boileau E**, **Nithiarasu P**, **Blanco PJ**, **Müller LO**, **Fossan FE**, **Hellevik LR**, **Donders WP**, **Huberts W**, **Willemet M**, **Alastruey J.** A benchmark study of numerical schemes for one-dimensional arterial blood flow modelling. *Int J Numer Method Biomed Eng* 31: e02732, 2015. doi:10.1002/cnm.2732.
55. **Leguy CA**, **Bosboom EM**, **Belloum AS**, **Hoeks AP**, **van de Vosse FN.** Global sensitivity analysis of a wave propagation model for arm arteries. *Med Eng Phys* 33: 1008–1016, 2011. doi:10.1016/j.medengphy.2011.04.003.
56. **Stein M.** Large sample properties of simulations using Latin hypercube sampling. *Technometrics* 29: 143–151, 1987. doi:10.1080/00401706.1987.10488205.
57. **Quicken S**, **Donders WP**, **van Disseldorp EMJ**, **Gashi K**, **Mees BM**, **van de Vosse FN**, **Lopata RG**, **Delhaas T**, **Huberts W.** Application of an adaptive polynomial chaos expansion on computationally expensive three-dimensional cardiovascular models for uncertainty quantification and sensitivity analysis. *J Biomech Eng* 138: 121010, 2016. doi:10.1115/1.4034709.
58. **Laurent P**, **Albaladejo P**, **Blacher J**, **Rudnichi A**, **Smulyan H**, **Safar ME.** Heart rate and pulse pressure amplification in hypertensive subjects. *Am J Hypertens* 16: 363–370, 2003. doi:10.1016/S0895-7061(03)00063-3.